Colour Algorithms for Monotonic Nonlinear CMOS Image Sensors

by

Syed Hussain

A thesis submitted in partial fulfillment of the requirements for the degree of

Master of Science

in

Signal and Image Processing

Department of Electrical and Computer Engineering

University of Alberta

Abstract

Compared to human vision, dynamic range (DR) is a limiting factor for modern cameras. While conventional complementary metal-oxide-semiconductor (CMOS) image sensors are limited in their ability to capture DR, nonlinear CMOS image sensors, e.g., with logarithmic (log) or linear-logarithmic (linlog) responses, are able to capture high/wide DRs in single exposures at video rates. Considering the drawbacks of such sensors, this thesis proposes and validates new algorithms, for colour correction and demosaicking, that are specially designed for nonlinear sensors where the response is a monotonic function of stimulus, a property of log and linlog sensors. The proposed colour correction has a nonlinear part, which employs cubic Hermite splines, followed by a linear part. To estimate relevant parameters, calibration with a colour chart is required. The method is validated, through simulation, using a combination of experimental data, from a monochromatic log sensor, and spectral data, from the literature. The proposed nonlinear demosaicking uses weighted medians to filter pixels exhibiting salt-and-pepper noise (SPN), a drawback of nonlinear sensors, while determining a colour for each channel at every pixel. Variations of the method are considered and evaluated. To produce mosaicked images for testing, a Kodak true colour image set is subsampled, in a Bayer colour filter array pattern, and SPN of varying densities is added. Results of the proposed method are compared to those from a popular literature method. Finally, future directions of this work are discussed, such as a fixed-point implementation of both algorithms and ways to facilitate additional experimental results.

Preface

Chapter 2 of this thesis has been published, after peer review of the entire work, as Syed Hussain and Dileepan Joseph, "Spline-Based Colour Correction for Monotonic Nonlinear CMOS Image Sensors," *Proceedings of the IS&T International Symposium on Electronic Imaging*, 362 (2019).

In Chapter 2, Hussain was responsible for the design, implementation, validation, and evaluation of the algorithm, with advice from Joseph. Hussain was also responsible for writing the Apparatus and Method, the Simulation Results, and the Conclusion sections. Hussain wrote the initial version of the Introduction section, including the opening abstract. Joseph revised these opening parts substantially, and edited the other sections.

The design, validation, and evaluation of the algorithm, proposed in Chapter 3, was completed by Hussain, with advice from Joseph. Both Hussain and Joseph implemented the algorithm independently. After he confirmed the results were identical, Hussain employed Joseph's implementation thereafter. The chapter was written by Hussain, and edited by Joseph.

All other parts of the thesis were written by Hussain and edited by Joseph. In particular, Joseph made significant edits to the Abstract.

Acknowledgements

I would firstly like to thank my supervisor, Dr. Dileepan Joseph, for all his efforts in supporting me in my program. Without him, this project would not have been possible. His considerable knowledge of electronic imaging, along with his patient teaching were invaluable to me during my time at his lab. I have gained skills that I did not even previously realize I lacked under his supervision.

I would also like to thank my family for their love and support during the completion of my degree. Additionally, I would like to thank the Faculty of Graduate Studies and Research, as well as the Graduate Students' Association for funding the Academic Travel Grant I was given. My research was also partly funded by a grant from the Natural Sciences and Engineering Research Council of Canada, for which I am very grateful. Lastly, the staff at the Cameron and Rutherford library were invaluable resources to me during my research, so I am greatly indebted to them.

Contents

List of Tables

List of Figures

Chapter 1

Introduction

The class of complementary metal-oxide-semiconductor (CMOS) image sensors offers high speed and functionality as an alternative to charge coupled device (CCD) image sensors. One drawback to traditional CMOS image sensors is that their dynamic range (DR) is relatively low compared to human vision. Nonlinear image sensors have been shown to capture a wider DR than linear CMOS image sensors at video rates. The benefits of high/wide dynamic range (HDR) CMOS image sensors have the potential to make significant contributions to various industries. However, nonlinear image sensors, such as logarithmic (log) or linear-logarithmic (linlog) image sensors, tend to behave differently than linear image sensors when encountering similar problems and therefore need to be handled separately. Some of these problems can be addressed with image signal processing. In particular, because colour is such an essential component of imaging, colour correction algorithms for nonlinear image sensors need to be developed to properly handle the nonlinearity of the sensor response. Additionally, demosaicking algorithms need to be revisited to make them more suitable for producing colour images captured by nonlinear image sensors.

1.1 High/Wide Dynamic Range Imaging

Image sensors capable of HDR imaging are a promising solution to improve the DR of image sensors. Similar to how the imaging industry has largely migrated from CCD image sensors to CMOS image sensors, the benefits provided by

nonlinear CMOS image sensors have the potential to shift the focus of imaging technology. Image sensors are used in a myriad of industries. The range of applications can be extended tremendously, according to the literature, by replacing traditional image sensors with HDR imaging technology.

1.1.1 Applications and Opportunities

In recent years, image sensors have become prevalent in society. As the technology behind image sensors continues to improve, CCD image sensors are being replaced by CMOS image sensors, allowing CMOS image sensors to become the dominant imaging technology [4]. CMOS image sensors have traditionally been favoured over CCD image sensors because they exhibit lower power dissipation, more portability, and generally lower prices [13]. Consequently, various applications, including cell phones, video cameras, digital single-lens reflex (DSLR) cameras, are adopting CMOS image sensors [40]. However, one distinct disadvantage traditional CMOS image sensors have is that they are less sensitive to light than CCD image sensors of the same pixel size [5], [43]. Tomoyuki Suzuki, Senior Vice-President of Sony, stated in his plenary talk at the ISSCC 2010 that the next step for CMOS image sensors is to exceed human vision [40].

In order for this to be possible, improvements have to be made in several aspects of image sensors. In their comprehensive review of modern cameras, Skorka and Joseph found that the DR was the limiting factor compared to the human visual system, followed by the dark limit [37]. The DR of an imaging system is the range of luminances that the system can accurately capture, with the dark limit defining the lower end of the range, and the bright limit defining the upper end. Skorka and Joseph define the dark limit as the lowest luminance at which the signal-to-noise-and-distortion ratio (SNDR) exceeds 0 dB, and the bright limit as the highest luminance that does the same. Beyond these limits, the system cannot accurately interpret the signals received by the image sensors. Figure 1.1 shows a comparison of the performance of the human eye versus several image sensors in regards to the DR and the dark limit. These results indicate that the human eye is superior to most image sensors in both

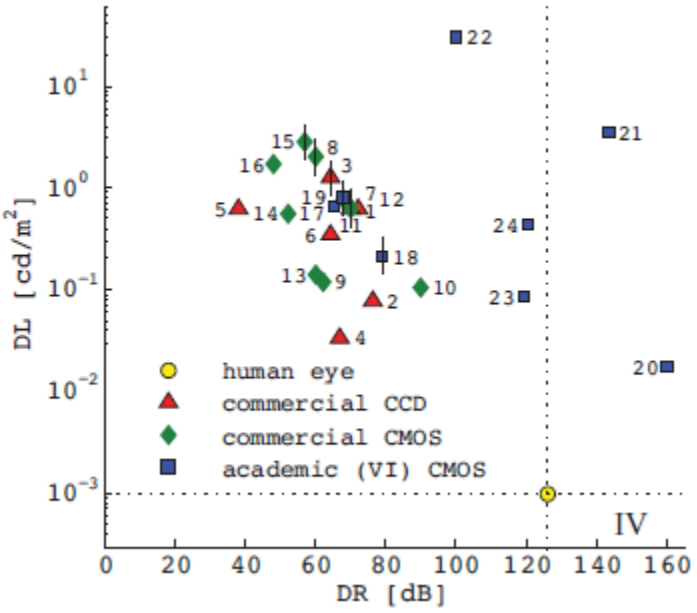

Figure 1.1: Dark limit and dynamic range of modern image sensors. Skorka and Joseph show that most image sensors are well below the standard of the human visual system in terms of dark limit and intra-scene DR. The marked quadrant indicates which region performance would be superior to the human eye. Taken from Skorka and Joseph [37].

aspects.

Figure 1.2 shows the range of intensities that may be encountered in the real world, which is called the inter-scene DR. Considering that the intra-scene DR can exceed 6 orders of magnitude [37], it becomes important to design pixels that can accurately interpret incoming light signals over a high/wide DR of intensities. The field of study that deals with designing and implementing such imaging systems is known as HDR imaging. Properly handling HDR data means information that may otherwise be lost is retained due to pixels remaining unsaturated, as evidenced by Fig 1.3. Unsurprisingly, HDR imaging has generated a lot of interest, as it promises a great deal of benefit in various fields of application.

The medical imaging industry has benefited tremendously from the advances made in CMOS imaging technology. CMOS image sensors have be-

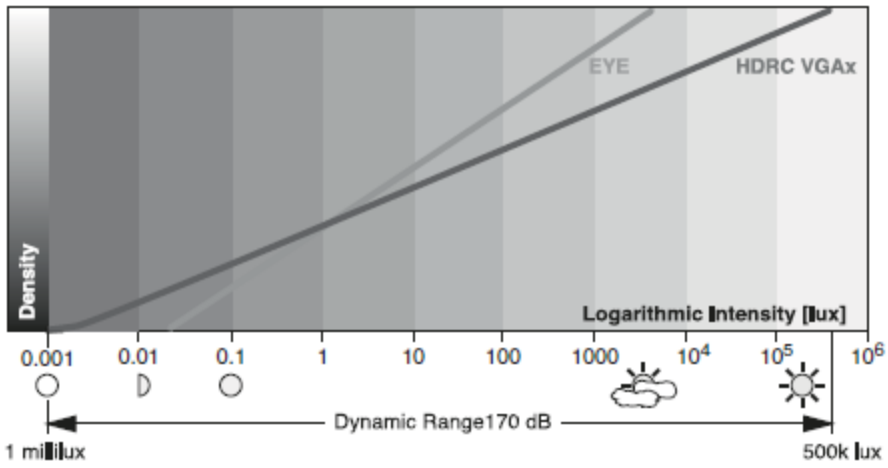

Figure 1.2: Range of intensities possible in the real world. The response of the human eye is given along with the HDR response of a log sensor. Taken from Hoefflinger [15].

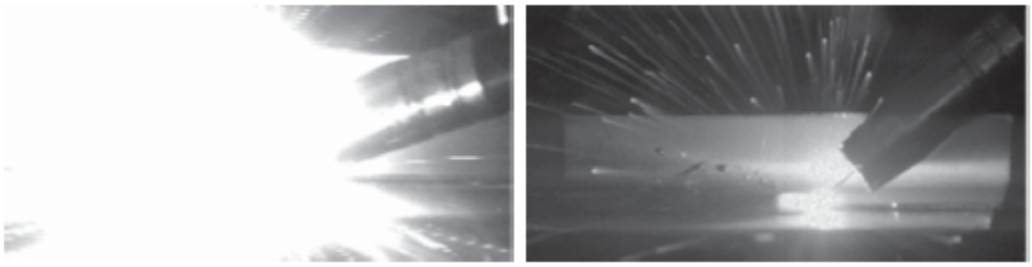

Figure 1.3: Images from a CCD camera and an HDR camera. The difference in the quality of the two images shows the advantages of using HDR cameras. Because pixels are not as easily saturated, more detail from the scene can be captured. Taken from Hoefflinger [15].

come a viable option for real-time digital X-ray imaging, as opposed to the traditional amorphous silicon (a-Si) flat panel imagers used previously. Ganguly *et al.* [11] describe an implementation of a CMOS X-ray detector that is capable of operating at high/wide DR. CMOS X-ray imagers have several advantages over a-Si flat panel imagers. These imagers have a faster readout speed and lower noise. The lower noise allows for higher/wider DR, while the faster readout results in quicker scanning, which is especially important for procedures where the patient may have to hold their breath [45]. As opposed to traditional X-ray imaging, which is a monochromatic operation, techniques have been developed that create coloured two-dimensional X-ray images using

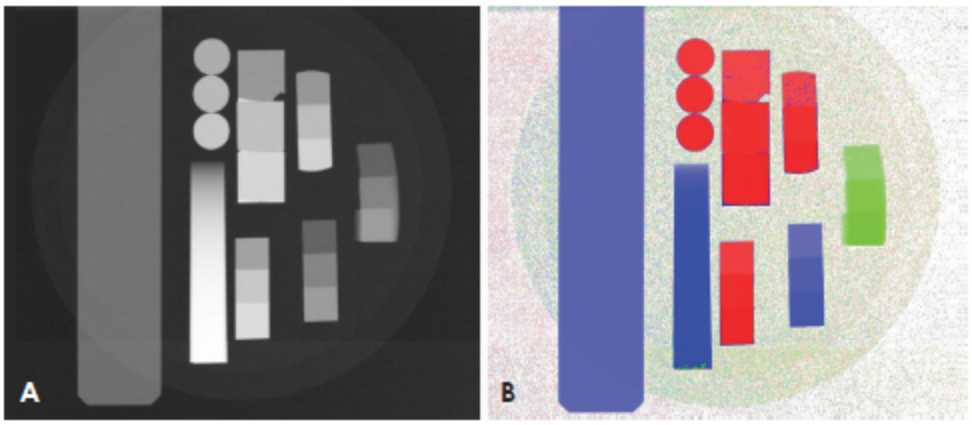

Figure 1.4: Traditional and colourized X-ray. The image contains objects of different materials. While the traditional method produces a grayscale image, the dual-energy method is able to produce a coloured image that can correctly differentiate between the different materials in the scene. Taken from Peter *et al.* [32].

multispectral X-ray imaging. Peter *et al.* [32] develop a method of colorizing a dental X-ray image by exposing the material to two different X-ray spectra. By comparing the material's response to the two different spectra, they were able to classify, and colourize, different materials provided both X-ray spectra were able to penetrate the samples. The possibility of combining multispectral X-ray imaging with HDR X-ray image sensors would allow for greater range and accuracy of classification of materials.

In addition, HDR CMOS image sensors have made promising contributions to the automotive industry. With the advent of autonomous vehicles, it is increasingly important that reliable and accurate data is available to the various algorithms that govern the actions of the vehicles. Despite the reduced traffic volume at night, about 46% of driving fatalities occur at night [14]. Dim lighting reduces human drivers' abilities to avoid collision [33]. HDR imaging is a promising solution. HDR cameras are more robust against saturation from bright scenes. Fig 1.5 shows a possible scene viewed by a vehicle. The image on the right, taken by an HDR camera, contains significantly more details than the image on the left, which is taken by a linear camera. This highlights the superiority of using HDR image sensors for automotive applications.

Figure 1.5: Automotive camera vision using linear and HDR cameras. Automotive algorithms depend on the information obtained from cameras to make decisions about the actions of the vehicle. Proper information has to be given to the algorithm in order to operate successfully. Taken from Hertel and Chang [14].

A current alternative to using cameras in autonomous vehicles is LIDAR. However, while LIDAR is more accurate, Stein *et al.* show that cameras are sufficient in implementing adaptive cruise control (ACC) [38]. In addition, a camera-based ACC system would be cheaper to bring to production compared to a LIDAR-based system. Often, the main weakness cited for using traditional CMOS image sensors is their inability to handle illumination variances, and their night vision difficulties [30]. HDR image sensors, however, are significantly better at addressing these issues.

1.1.2 Technology and Challenges

It is possible to obtain HDR images using linear image sensors by taking multiple shots with varying exposure settings. However, this multiple sampling method is best applied to static scenes. For dynamic scenes or video applications, motion artifacts will appear in the final result. Due to their linear response to incoming light, linear image sensors are only capable of capturing a limited DR, which results in poor quality images for scenes with a high/wide DR [41]. Image sensors with a nonlinear response to incoming light have the potential to capture HDR images in a single shot, because pixels are less susceptible to saturation. In particular, image sensors with a log response to incoming light have been developed that demonstrate DRs greater than 120 dB. However, a problem often associated with log sensors is that they

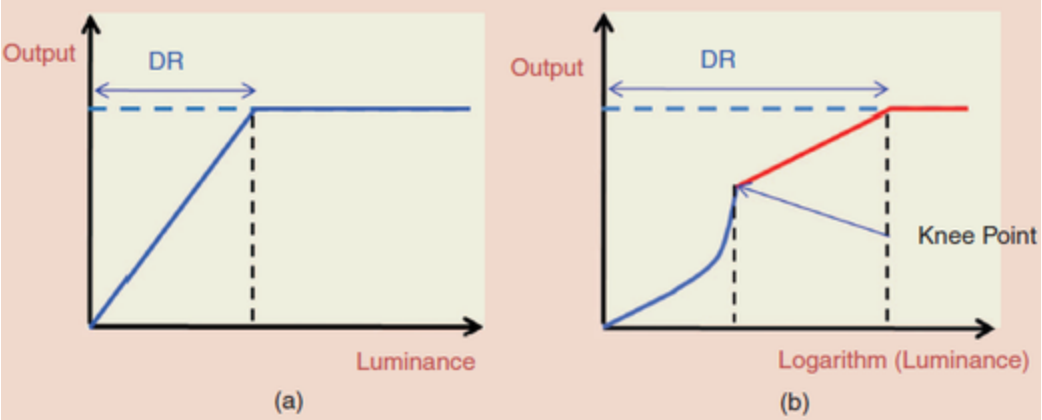

Figure 1.6: Responses of linear and linlog image sensors. (a) A typical OECF of a linear image sensor. (b) A typical OECF of a linlog image sensor. One axis of the linlog graph is shown on a log scale. The DR of the image sensor increases dramatically due to the log response after the knee point. Taken from Kim [20].

have small voltage swings. This limited range of voltage output results in low signal-to-noise ratios (SNRs). Lai *et al.* [25] developed a CMOS image sensor that addressed this issue by increasing the voltage swing to 1 V. Improving on this result, Campos *et al.* [8] showed an implementation of a log CMOS image sensor with a voltage swing of 2.65 V over a range of 120 dB by using up to four transistors in series.

Linear-logarithmic (linlog) image sensors are another popular type of non-linear image sensor capable of high/wide DR. These image sensors extend the DR of a linear image sensor by using a log response when the output value of the pixel reaches a certain limit, and a linear response on the lower luminances, which decreases the dark limit. Figure 1.6 shows a typical opto-electronic conversion function (OECF) of a linlog sensor as well as a linear sensor. It is evident from the figure that the DR is extended significantly due to the log response. One drawback to this configuration is that it becomes very difficult to model this type of response. In the literature, there are several examples of image sensors that use the linlog architecture. Li *et al.* propose a pixel with two modes: a linear response mode and a log response mode [24]. They report a DR of 161 dB. Bae *et al.* use a similar dual-mode architecture to achieve a DR greater than 106 dB [1]. Regardless of the particular configuration of the

image sensor, nonlinear image sensors show strong potential for being able to capture scenes with a high/wide DR.

Despite their numerous advantages, there are drawbacks to the log and linlog CMOS image sensors. This class of imagers has been known to exhibit high levels of fixed pattern noise (FPN), a spatial as opposed to temporal noise that is the result of device parameter mismatch. Although all the pixels in the sensor are made together, variations in the manufacturing process of the sensor can cause each pixel to respond differently to the same stimulus. Correcting FPN for a log image sensor can be done using a model of the image sensor response. One such model is the offset, gain, and bias (OGB) model [18], which requires parameters for the specific camera to be determined via a calibration process. While this can be applied to log image sensors, linlog image sensors have a more complicated response, which cannot be modeled as easily. In their recent paper, Nascimento *et al.* [31] describe and implement a digital circuit method that is able to perform FPN correction, on an arbitrary image sensor, by using Li *et al.*'s [23] generic model. This model makes no assumptions about the response of the image sensor except that it is monotonic, a desirable property for any image sensor. The method uses a cubic Hermite spline to interpolate between data points.

Whereas spline interpolation is non-monotonic, a cubic Hermite spline is able to preserve the monotonic nature of the data [6]. As Fig 1.7 shows, spline interpolation creates oscillations that destroy the monotonicity of the curve. This would be problematic for an imaging system, which uses interpolation to correct responses, so a cubic Hermite spline is the preferred interpolating method. Li *et al.* use this approach to model the photometric response of an arbitrary image sensor. They also show how the monotonicity property suffices to develop an effective method for FPN correction. Nascimento *et al.* implemented the FPN correction method using digital circuits, and showed that their approach outperforms competing analog, mixed-signal, and digital circuit methods in the literature.

Another type of noise that is associated with nonlinear image sensors is salt-and-pepper noise (SPN). Traditionally, SPN occurs because there is some

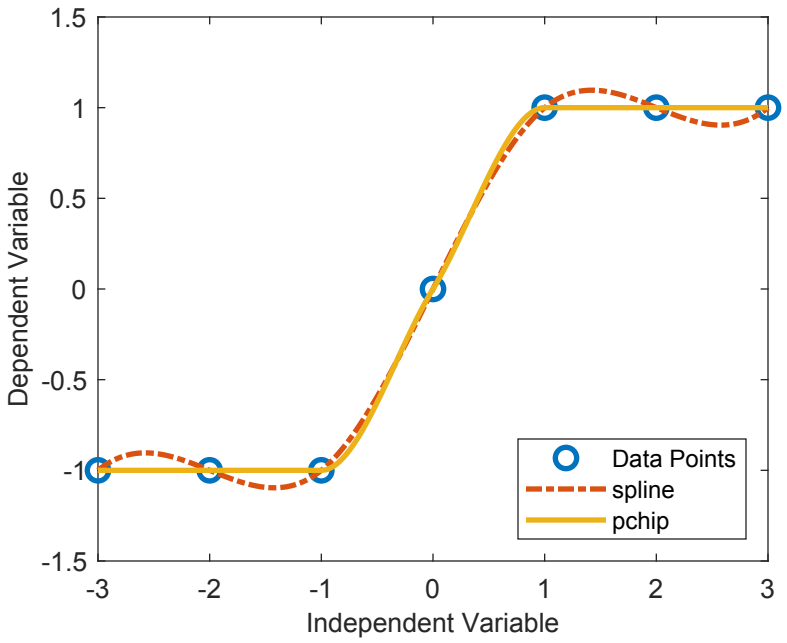

Figure 1.7: Spline versus cubic Hermite spline interpolation. Spline interpolation results in a non-monotonic function, whereas piecewise cubic Hermite spline, or pchip, interpolation is able to preserve the monotonicity of the data. This is important when the interpolated data is a model for the response of an image sensor, which is monotonic in nature. Figure based on MATLAB example.

defect in the image sensor that causes a pixel to be always bright, or always dark, regardless of the light conditions. These pixels have a largely different response to stimulus than those in their local neighborhood [44]. Although it is possible to detect and locate the exact pixels in the image that cause this error, it is not the only solution in the literature. Instead, a noise reduction algorithm can be applied to the entire image. SPN behaves differently in nonlinear image sensors than it does for linear image sensors [31]. For linear image sensors, SPN is a static noise. Pixels "stuck" at certain values can be identified and corrected. However, for nonlinear image sensors, SPN becomes dynamic. Pixels may appear defective at some luminances and become active at different luminances. Unlike FPN correction, which requires calibration, SPN correction can be implemented by applying a filter after other correction algorithms have been implemented. Median filtering is an effective solution

for SPN correction, as it uses the fact that defective pixels are outliers [22]. Nascimento *et al.* show that a median filter approach is not only feasible, but efficient, in circuit-based methods for removing SPN.

With all the research being done with nonlinear image sensors, one area that has not been given enough attention is colour. Integrating colour into images is a logical next step for nonlinear image sensors. Colour is a core aspect of visible-band imaging, yet research on nonlinear image sensors, for the most part, focuses on the monochromatic case. Aside from producing more visually pleasing images, colour also allows for more information to be encoded into images being captured. Similar to FPN correction, colour correction is an operation that requires a calibration process. For linear image sensors, colour correction is the process of applying a linear matrix transform on a tristimulus pixel value to convert the data from a device-dependent camera space to a standard device-independent space. Calibration is required to determine the parameters for the transform. This technique is insufficient for nonlinear image sensors, as evidenced by previous work in the area by Joseph and Collins [19].

1.2 Image Processing Pipeline

Having the correct circuit configuration on an image sensor is not sufficient in displaying a full HDR image. Images taken from a sensor have a series of operations performed on them to optimize the images for a particular objective. This series of operations, called the image processing pipeline, is performed by circuitry in real time after the data from the image sensor is collected. Below, we consider two operations that are integral to converting an image from a grayscale image to a colour image.

1.2.1 Colour Correction

Raw data from an image sensor is collected as unsigned integers. The interpretation of these integers is dependent on the circuitry of the image sensor. The raw data is considered to be in camera space, which is a device specific representation. A colour correction algorithm is used to transform the cap-

tured images from the camera space to a standard, device independent, colour space, e.g., CIE XYZ. From CIE XYZ, there are transforms that can alter the data so that it can be displayed, or analyzed. Linear colour correction is done using a 3×3 matrix to transform a tristimulus pixel value from one space to another. The matrix is determined using a calibration process, where images with known colours are shown to the camera. Using matrix operations, a transform between the camera space and the CIE RGB space can be determined. The transform, in general, will not be a perfect transform because that would imply that the colour filter array (CFA) transmission functions are a linear combination of the CIE RGB functions.

This technique of colour correction cannot be applied directly to nonlinear image sensors because the response of nonlinear image sensors can be very different depending on the luminance. A relatively minor change in luminance can change the output of the image sensor disproportionately. This will skew the results of the linear transform. An alternate method is needed to handle the nonlinear aspect of nonlinear image sensors. This thesis proposes a novel technique to perform colour correction on images captured by nonlinear image sensors. By separating the colour correction algorithm into nonlinear and linear colour correction stages, this thesis shows that colour correction for nonlinear image sensors is not only possible, but achieves excellent results.

1.2.2 Demosaicking

For standard CMOS image sensors, colour is incorporated by placing a CFA over the image sensor, and then applying some form of interpolation to obtain red, green, and blue values for all pixels in the sensor. Because each pixel only captures one colour depending on the CFA, a demosaicking algorithm is applied to estimate the missing colour components at each pixel location. A common CFA used in CMOS image sensors is the Bayer CFA [7]. This particular configuration is composed of a repeating block of four pixels: two green pixels for every red and blue pixel. The green pixels are sampled twice to reflect the higher sensitivity of the human visual system to the colour green. Figure 1.8 shows a typical arrangement of the elements in a CMOS image

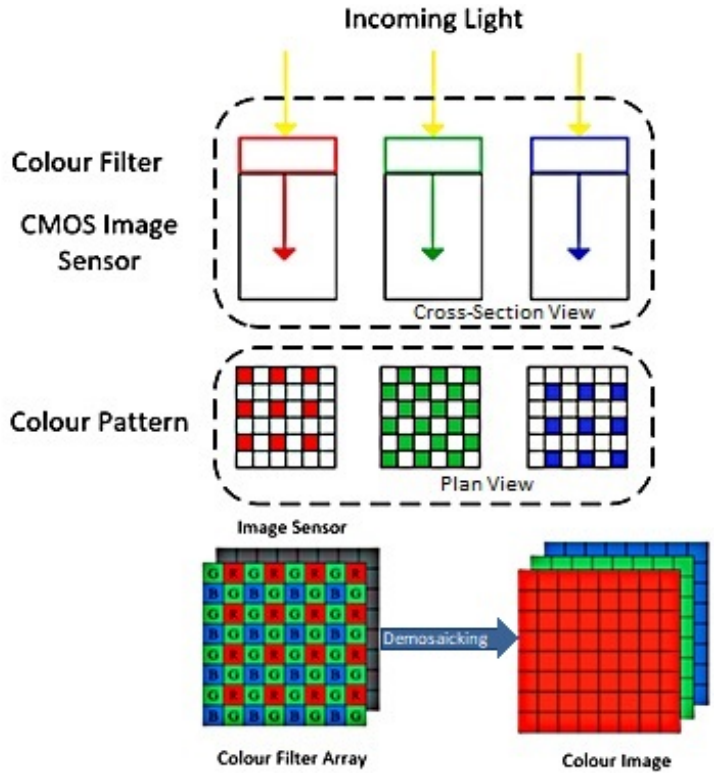

Figure 1.8: A colour CMOS image sensor with a Bayer CFA. Incoming light passes through either a red, green, or blue filter and generates a colour stimulus pattern on the pixel array. Interpolation is required to realize a full colour image. Adapted from Selek [35].

sensor. Demosaicking is a process that can, for the most part, be decoupled from other processes in the image processing pipeline. It is generally performed before data from the camera has been converted to a standard colour space. As such, methods used for demosaicking linear CMOS image sensors can be readily applied to nonlinear CMOS image sensors.

There are various methods of demosaicking suggested in the literature. Bilinear interpolation is a very simple form of demosaicking. Another simple form is to use a nearest neighbours approach. However, a drawback to such methods is that they may cause artifacts in the images [27], especially in regions with sharp edges where colour gradients are high. In an effort to optimize performance along edges, Kimmel [21] uses edge detection to specifically target areas with high colour gradients. The interpolation along these regions is weighted by a function of the directional derivatives to reduce the effect of the

large colour contrasts.

Due to its popularity, there are many methods proposed that consider only the Bayer CFA in order to simplify the process. Malvar *et al.* proposes a linear demosaicking algorithm that has been adapted by MATLAB for their Image Processing Toolbox [27]. The method uses a sliding window algorithm with weighted masks to compute a modified bilinear interpolation operation on every pixel in the image. An important aspect of this work is that it is a simple functional mapping, which allows it to be computationally efficient in addition to being a linear mapping. Because previous algorithms search for regions of high colour gradients, they involve selection in addition to nonlinearity. Malvar *et al.* apply a corrective term to each interpolated pixel. The corrective term is a measure of the change in luminance at the pixel. This allows the interpolation at every pixel to be sensitive to edges in the image, without explicitly performing edge detection.

While the techniques mentioned above are relevant for nonlinear image sensors, it is important to consider that nonlinear image sensors suffer from SPN. Demosaicking is inherently a spreading operation: it attempts to populate a larger set using data from a smaller set. In the absence of SPN, this is not problematic if done correctly. However, when SPN is present, demosaicking algorithms can spread defective pixel values to other pixels, decreasing the quality of the entire image. For nonlinear image sensors, it is important to consider SPN when demosaicking to make sure only valid pixel values are considered. This thesis proposes and validates a method of demosaicking that simultaneously filters SPN. The method is validated against a leading literature approach, namely Malvar *et al.*'s method, and we show that in the presence of SPN, our proposed method outperforms the competition.

1.3 Scope of Work

There are many aspects of HDR imaging that can be considered. This thesis proposes and evaluates two methods whose ultimate goal is to display colour images taken from nonlinear CMOS image sensors. Chapter 2 proposes a

colour correction method for images taken by a monotonic nonlinear CMOS image sensor. First, we explain the motivation for the proposed algorithm. Next, we present a background for the work, as well as the ideas that the proposed algorithm is based on. While the algorithm presented is applicable to any type of monotonic nonlinear CMOS image sensor, this work validates the proposed method using data from a log sensor developed by Mahmoodi *et al.* [26]. Nevertheless, the algorithm makes no assumptions that the sensor response is anything other than monotonic. Because we use a simulation-based approach to validate our results, we build a model of an image sensor containing all details relevant to our scenario. We then present a series of results that show that our method is capable of performing colour correction accurately.

In Chapter 3, we look at the challenges in demosaicking images captured by nonlinear image sensors. First, we present the motivation for combining the demosaicking and SPN filtering operations. We then go over the ideas upon which the proposed method is built, before presenting our method. We also present variations of the method to help explain its properties. For validation, we test against the results of Malvar *et al.*

Finally, in Chapter 4, we conclude with summarizing our motivations, as well as the methods presented in this thesis. We highlight the novelty and significance of the methods presented, and we show that both methods are successful in achieving the goals defined for them. Lastly, we discuss future plans for the work presented in this thesis.

Chapter 2

Colour Correction

Nonlinear complementary metal-oxide-semiconductor (CMOS) image sensor (CIS) technology is capable of high/wide dynamic range (DR) imaging at high frame rates without motion artifacts. However, unlike with linear CIS technology, there is no generic method for colour correction of nonlinear CIS technology. Instead, there are specific methods for specific nonlinear responses, e.g., the logarithmic (log) response, that are based on legacy models. Inspired by recent work on generic methods for fixed pattern noise (FPN) and photometric correction of nonlinear sensors, which depend only on a reasonable assumption of monotonicity, this chapter proposes and validates a generic method for colour correction of nonlinear sensors. The method is composed of a nonlinear colour correction, which employs cubic Hermite splines, followed by a linear colour correction. Calibration with a colour chart is required to estimate the relevant parameters. The proposed method is validated, through simulation, using a combination of experimental data, from a monochromatic log CIS, and spectral data, reported in the literature, of actual colour filter arrays (CFAs) and target colour patches.

2.1 Introduction

CISs have become the dominant imaging technology, with charge coupled devices (CCDs) comprising less than 10% of the market share since 2010 [4]. Research in the area includes work on nonlinear sensors, such as log and linear-logarithmic (linlog) ones [1], [3]. It is well known they can achieve a high/wide

DR in single exposures at video rates and, with the work of Mahmoodi *et al.* [26], also to realize a high peak signal-to-noise-and-distortion ratio (PSNDR).

Recent work on nonlinear sensors does not address colour specifically. Brunetti and Choubey [3] alter the log sensor circuit to improve its sensitivity in the dark. Meanwhile, Bae *et al.* [1] develop a variation of the linlog circuit with two piecewise linear regions in the dark. Given that colour is an integral component of visible-band imaging technology, one can safely assume from the ongoing interest in nonlinear sensors that legacy work on colour correction in such sensors is worth improving upon.

The main limitation of legacy work on colour correction, in nonlinear sensors, is that it is specific to the classic log sensor. Methods by Hoefflinger [15] and Joseph and Collins [19] rely on a classic model of the log sensor, developed by Joseph and Collins [18] for FPN correction. While these colour correction methods worked to some degree, they are not applicable to the variety of nonlinear sensors of interest today, including log sensor variations that deviate from the classic model.

This chapter proposes a new approach to colour correction, which leverages a model recently developed by Li *et al.* [23], using low-degree polynomials and cubic Hermite splines, for FPN and photometric correction. Relying only on the monotonicity of pixel responses, this model is so generic that it may be applied to a wide variety of sensors, including log and linlog variations. Also, Li *et al.* [23] showed that, when applied to Mahmoodi *et al.*'s log sensor [26], FPN correction using the generic model was competitive with FPN correction using the classic specific model.

One difficulty of working on this subject is the challenge of obtaining experimental data from a nonlinear image sensor, i.e., an array of nonlinear pixel sensors, having a CFA. Therefore, we adopt a simulation strategy here by using monochromatic experimental data, from Mahmoodi *et al.*'s documented image sensor [26], and spectral data from multiple literature sources, regarding the quantum efficiency (QE) of photodiodes, the transmittance of a CFA, and the reflectance of a wide variety of objects, to validate our proposed method.

We first summarize the apparatus of interest, i.e., a nonlinear sensor that

obeys the assumptions laid out by Li *et al.* [23]. However, we extend Li *et al.*'s model from a monochromatic to a colour scenario. Thereafter, the new colour correction method is proposed, which entails a description also of colour calibration. Because FPN is inherent to nonlinear sensors and Li *et al.*'s model, we review FPN, its calibration, and its correction, focusing on implications for colour calibration and correction.

Moreover, we present a suite of results to validate and evaluate the proposed method, including two variations thereof. They include calibration with Macbeth chart patches and testing with a large database of other patches. Not only do we report median 1976 Commission Internationale de l'Éclairage (CIE) L*a*b* (CIELAB) errors, including over a high/wide DR, but also their probability density functions (PDFs). Errors are broken down into luminance and chromaticity parts, and are compared to just noticeable difference (JND) thresholds.

We conclude the chapter by summarizing our motivation, apparatus, methods, results, and discussion. Our conclusion also highlights the novelty and significance of this work—a generic method for the colour correction of nonlinear sensors.

2.2 Apparatus and Method

This chapter proposes and validates a method to correct colour for the class of image sensors that are strictly nonlinear and monotonic in their response to incoming light. It is intended to be implemented, in real time, as one subsystem in a series of subsystems of an image processing pipeline. It is designed to output images in the 1931 CIE XYZ (XYZ) colour space. These may be easily transformed into other colour spaces.

Figure 2.1 illustrates a nonlinear imaging system, comprising a nonlinear image sensor and an image processing pipeline for FPN and colour correction. A transformation to the sRGB colour space, suitable for display, is indicated at the output.

The proposed method has two stages. The first is calibration, which is

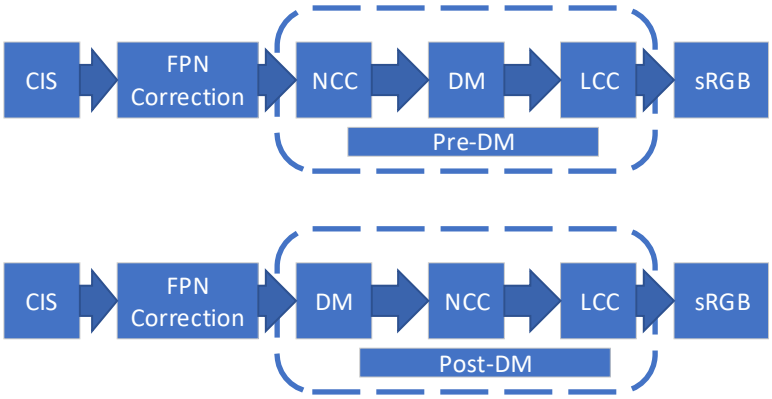

Figure 2.1: The proposed colour imaging system. Dashed boxes indicate the focus of our work. Nonlinear colour correction (NCC) is done before or after demosaicking (DM). They are followed by linear colour correction (LCC).

performed once to establish parameters required in the correction stage. Correction is then performed, in real time on all frames, using a combination of nonlinear and linear colour corrections. Assuming the image sensor uses a CFA, demosaicking is also needed. Variations in the sequence of performing the colour corrections and demosaicking yield different results.

Below, we first analyze relevant aspects of image sensors. Next, taking nonlinear and linear parts separately, the proposed colour correction method is explained, calibration included. For demosaicking, we simply use Malvar *et al.*'s [27] algorithm.

2.2.1 Image Sensor

An imaging system views an object when a spectrum of light reflects off a scene and hits an array of pixels. In a given pixel array, the circuit configuration of the pixels will not vary, but due to variations in device manufacturing, responses to identical input can vary from pixel to pixel. This is the basis of FPN.

Considering FPN and nonlinearity, to describe the response of the jth pixel, in an array of pixels, we can write:

$$y_j = f_j(x_j) + \epsilon_j, \tag{2.1}$$

where f_j is the opto-electronic conversion function (OECF) of the pixel, ϵ_j is a

noise associated with each pixel that encapsulates temporal and quantization noise, and x_j is the stimulus.

The stimulus x_j, of the jth pixel, depends on localized scene illumination and object reflectance, as well as CFA transmission and photodiode sensitivity. It can be modeled as follows:

$$x_j = \int_0^\infty s_j(\lambda)\beta_j(\lambda)\alpha_j(\lambda)d\lambda, \tag{2.2}$$

where s_j, β_j, and α_j, which are functions of wavelength λ, are the illumination, reflectance, and absorption spectra. Whereas x_j and s_j can have dimensions, e.g., cd/m^2 and cd/m^2/nm, β_j and α_j are always dimensionless and range from 0 to 1.

Assuming R, G, and B represent, according to the CFA, the sets of pixels with red, green, and blue colour filters, respectively, the absorption spectrum may be modeled as follows:

$$\alpha_j(\lambda) = \begin{cases} T_{\mathrm{R}}(\lambda)Q(\lambda), & j \in R, \\ T_{\mathrm{G}}(\lambda)Q(\lambda), & j \in G, \\ T_{\mathrm{B}}(\lambda)Q(\lambda), & j \in B, \end{cases} \tag{2.3}$$

where T_{R}, T_{G}, and T_{B} are the transmission efficiencies of the red, green, and blue colour filters, and Q is the quantum efficiency of the photodiode. They are treated as constants because there are enough degrees of freedom, in (2.1), to model FPN.

The proposed method requires that f_j, the OECF in (2.1), be a monotonic function. Monotonicity is a typical characteristic of any image sensor, including linear, log, and linlog. Although we use data from a log sensor, for validation purposes, the method is mathematically applicable to linlog and other possible high/wide DR sensors. The success of the method depends neither on the form of the OECF nor on its variation from pixel to pixel.

2.2.2 Nonlinear Correction

We assume FPN correction, shown in Fig. 2.1, is implemented using a polynomial-based method our lab previously published [23]. In that paper, our lab also

introduced a spline-based method for photometric correction. We amend and extend those methods, in this chapter, to realize a nonlinear colour correction.

Considering the pre-demosaicking variation, shown in Fig. 2.1, nonlinear colour correction follows FPN correction. During FPN calibration, an average response is computed as follows:

$$\bar{y}_i = \frac{1}{n} \sum_{j=1}^{n} y_{ij}, \tag{2.4}$$

where y_{ij} is the response to a uniform stimulus x_i, which varies, and n is the number of pixels. The averaging, in (2.4), reduces the significance of ϵ_j, in (2.1). The noise may be reduced further by averaging, for each stimulus x_i, over multiple frames.

Data points $(x_i, \bar{y}_i)$, from FPN calibration, are used to define F, an ideal monotonic and nonlinear OECF, as follows:

$$\bar{y}_i = F(x_i) \equiv \frac{1}{n} \sum_{j=1}^{n} f_j(x_i). \tag{2.5}$$

Our FPN calibration also computes n low-degree polynomials P_j, which are used to implement FPN correction as follows:

$$\hat{y}_j = P_j(y_j) \approx F(x_j), \tag{2.6}$$

where x_j and y_j are the stimulus and response, in (2.1), and $\hat{y}_j$ is the corrected response, i.e., the FPN correction output.

Our photometric correction computes an estimated stimulus, $\hat{x}_j$, using the corrected response, $\hat{y}_j$, as follows:

$$\hat{x}_j = \exp(S^{-1}(\hat{y}_j)) \approx F^{-1}(\hat{y}_j), \tag{2.7}$$

where S^{-1} is a cubic Hermite spline [6] fitted to the data points $(\ln x_i, \bar{y}_i)$ in the inverse direction. Logarithms are used to robustly deal with a high/wide DR on the x-axis. Unlike a cubic spline, a cubic Hermite spline guarantees monotonicity.

The stimulus x_i, in (2.5), is constant for all pixels, for a uniform scene imaged by a monochromatic sensor, because the absorption spectrum α_j equals

the quantum efficiency Q, in (2.3). However, for a uniform scene imaged by a colour sensor, the stimulus must be represented by three constants, as follows:

$$x_i^{\mathrm{R}} = s_i \int_0^\infty s_0(\lambda)\beta(\lambda)T_{\mathrm{R}}(\lambda)Q(\lambda)d\lambda, \tag{2.8}$$

$$x_i^{\mathrm{G}} = s_i \int_0^\infty s_0(\lambda)\beta(\lambda)T_{\mathrm{G}}(\lambda)Q(\lambda)d\lambda, \tag{2.9}$$

$$x_i^{\mathrm{B}} = s_i \int_0^\infty s_0(\lambda)\beta(\lambda)T_{\mathrm{B}}(\lambda)Q(\lambda)d\lambda, \tag{2.10}$$

where s_0 is the normalized illumination spectrum, e.g., a D65 spectrum in 1/nm, and s_i its photometric intensity, e.g., in cd/m^2. The R, G, or B superscripts indicate that the constants apply only to the red, green, or blue pixels, respectively.

Consequently, our previous FPN and photometric methods must be performed three times separately, once each for the red, green, and blue pixels. Instead of (2.6) and (2.7), we obtain:

$$\hat{y}_j = P_j(y_j) \approx \begin{cases} F_{\mathrm{R}}(x_j), & j \in R, \\ F_{\mathrm{G}}(x_j), & j \in G, \\ F_{\mathrm{B}}(x_j), & j \in B, \end{cases} \tag{2.11}$$

$$\hat{x}_j = \begin{cases} \exp(S_{\mathrm{R}}^{-1}(\hat{y}_j)) \approx F_{\mathrm{R}}^{-1}(\hat{y}_j), & j \in R, \\ \exp(S_{\mathrm{G}}^{-1}(\hat{y}_j)) \approx F_{\mathrm{G}}^{-1}(\hat{y}_j), & j \in G, \\ \exp(S_{\mathrm{B}}^{-1}(\hat{y}_j)) \approx F_{\mathrm{B}}^{-1}(\hat{y}_j), & j \in B, \end{cases} \tag{2.12}$$

where F_{R}, F_{G}, and F_{B} are ideal monotonic and nonlinear OECFs for red, green, and blue pixels, respectively, and S_{R}, S_{G}, and S_{B} are the cubic Hermite splines for the same. The splines may easily be created in normal or inverse directions, as indicated.

Thus, for the pre-demosaicking variation, the nonlinear colour correction is given by (2.12). It operates directly on the result, given by (2.11), of FPN correction. Each scalar $\hat{x}_j$ represents either a red, green, *or* blue value. After demosaicking, using the established algorithm by Malvar *et al.* [27], for each pixel there is a red, green, *and* blue value, which we may represent by a vector $\hat{\mathbf{x}}_j$.

Alternately, for the post-demosaicking variation, shown in Fig. 2.1, demosaicking happens after FPN correction. The result of FPN correction is still

a red, green, *or* blue scalar $\hat{y}_j$. It becomes a red, green, *and* blue vector $\hat{\mathbf{y}}_j$ after demosaicking. Thus, instead of (2.12), the nonlinear colour correction is as follows:

$$\hat{\mathbf{x}}_j = \begin{bmatrix} \exp(S_{\mathrm{R}}^{-1}(\hat{y}_j^{\mathrm{R}})) \\ \exp(S_{\mathrm{G}}^{-1}(\hat{y}_j^{\mathrm{G}})) \\ \exp(S_{\mathrm{B}}^{-1}(\hat{y}_j^{\mathrm{B}})) \end{bmatrix} \approx \begin{bmatrix} F_{\mathrm{R}}^{-1}(\hat{y}_j^{\mathrm{R}}) \\ F_{\mathrm{G}}^{-1}(\hat{y}_j^{\mathrm{G}}) \\ F_{\mathrm{B}}^{-1}(\hat{y}_j^{\mathrm{B}}) \end{bmatrix}, \tag{2.13}$$

where $\hat{y}_j^{\mathrm{R}}$, $\hat{y}_j^{\mathrm{G}}$, and $\hat{y}_j^{\mathrm{B}}$ are components of the vector $\hat{\mathbf{y}}_j$. The end result is a vector $\hat{\mathbf{x}}_j$ for either variation in Fig. 2.1.

2.2.3 Linear Correction

The input of the linear colour correction, shown in Fig. 2.1, is always a tristimulus vector, denoted $\hat{\mathbf{x}}_j^{\mathrm{RGB}}$, in the colour space of the nonlinear image sensor. Because nonlinear aspects are already corrected, the proposed linear colour correction proves identical to the colour correction of linear image sensors, i.e.,

$$\hat{\mathbf{x}}_j^{\mathrm{XYZ}} = \hat{\mathbf{D}}^{-1}\hat{\mathbf{x}}_j^{\mathrm{RGB}}, \tag{2.14}$$

where $\hat{\mathbf{x}}_j^{\mathrm{XYZ}}$ is the corrected tristimulus vector, in the standard XYZ colour space, and $\hat{\mathbf{D}}$ is a 3×3 matrix, which is invertible, that represents the underlying linear relationship.

Therefore, the novelty here is not in linear colour correction per se but rather in its calibration process, i.e., how $\mathbf{D}$ is estimated, because that is different compared to the linear image sensor case. One part of the calibration process remains the same. We require an image y_j of a standard colour chart, e.g., a Macbeth chart, illuminated by a standard illuminant, e.g., D65. After segmenting the image to isolate the colour chart patches, the true XYZ values, $\mathbf{x}_j^{\mathrm{XYZ}}$, of segmented pixels, $j \in C$, are known.

To estimate the unknown parameter $\mathbf{D}$, we minimize a sum of square errors (SSE), which is defined as follows:

$$SSE = \sum_{j \in C} (\hat{y}_j - Y_j)^2, \tag{2.15}$$

where $\hat{y}_j$ is the result, in (2.11), after FPN correction of the colour chart image y_j. For $j \in C$, Y_j is defined as follows:

$$Y_j = \begin{cases} S_R(\ln x_j^{\mathrm{R}}) \approx F_R(x_j^{\mathrm{R}}), & j \in R, \\ S_G(\ln x_j^{\mathrm{G}}) \approx F_G(x_j^{\mathrm{G}}), & j \in G, \\ S_B(\ln x_j^{\mathrm{B}}) \approx F_B(x_j^{\mathrm{B}}), & j \in B, \end{cases} \tag{2.16}$$

where S_R, S_G, and S_B are cubic Hermite splines that model ideal OECFs F_R, F_G, and F_B, as described previously, and x_j^{R}, x_j^{G}, and x_j^{B} are components of $\mathbf{x}_j^{\mathrm{RGB}}$. Due to a final equation, i.e.,

$$\mathbf{x}_j^{\mathrm{RGB}} = \mathbf{D}\,\mathbf{x}_j^{\mathrm{XYZ}}, \tag{2.17}$$

the scalar SSE, in (2.15), depends on the matrix $\mathbf{D}$.

As all relevant functions are differentiable, the gradient of the SSE with respect to $\mathbf{D}$, denoted ∇SSE, may be formulated. Using an established algorithm, such as `fminunc` in MATLAB, which terminates when ∇SSE equals the zero matrix, the SSE may be minimized. The matrix $\hat{\mathbf{D}}$ that minimizes the SSE is then used, in (2.14), to implement the linear colour correction.

2.3 Simulation Results

This section summarizes the results of testing the proposed method, and discusses the results achieved. First, we present details on how a colour nonlinear image sensor is simulated. Next, we describe how the image sensor is calibrated, and present the results of the calibration. Results of correction are then presented, including performance over a high/wide DR.

2.3.1 Image Sensor

The method is validated using a simulated colour log image sensor based on the model presented above. As with Li *et al.* [23], the OECF of the image sensor is determined by taking several images of uniform scenes of constant luminance.

Using literature data [10], [28], shown in Fig. 2.2, the stimulus x_j is simulated by evaluating (2.2) for each pixel, which has a colour filter on top of a

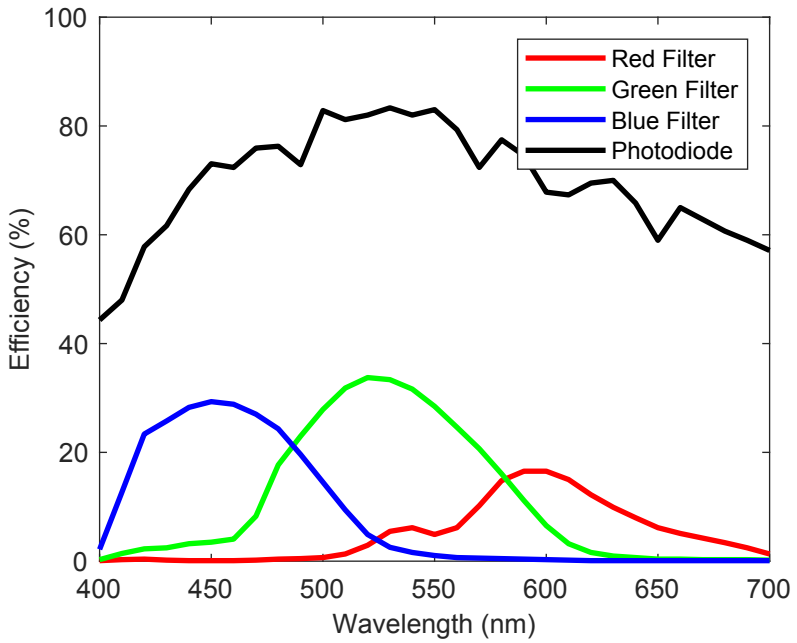

Figure 2.2: Transmission and quantum efficiency data from the literature. Red, green, and blue transmission efficiencies correspond to a Canon 5D CFA. The photodiode quantum efficiency is from a standard CMOS process. We use this data to help simulate a colour nonlinear image sensor.

photodiode, of the image sensor. The quantum efficiency $Q(\lambda)$ is a measure of the electron-hole pairs generated relative to photons, of a particular wavelength, incident on the photodiode. The colour filters are used to limit the wavelengths to a certain range and to weight them appropriately.

Assuming a standard Bayer CFA, we segment pixels into red ($j \in R$), green ($j \in G$), and blue ($j \in B$) sets. Using data from a monochromatic log image sensor, presented by Mahmoodi *et al.* [26], we compute red (S_R), green (S_G), and blue (S_B) cubic Hermite splines to model the ideal OECFs of red, green, and blue pixels, respectively, for colour calibration purposes. Inverse cubic Hermite splines are computed for colour correction.

As shown in Fig. 2.1, we focus on the colour correction part of a hypothetical nonlinear imaging system, in this case a log imaging system. Using Li *et al.*'s method, the FPN correction output, i.e., $\hat{y}_j$ in (2.6), is for each pixel equivalent to its ideal response, i.e., based on its ideal OECF, plus residual noise. According to Li *et al.*, the residual noise is proportional to the original

noise ϵ_j, in (2.1), and is normally distributed with zero mean.

Consequently, for each pixel of our colour log image sensor, we simulate the response to the stimulus as follows:

$$\hat{y}_j = \begin{cases} \text{round}(S_R(x_j) + \epsilon_j), & j \in R, \\ \text{round}(S_G(x_j) + \epsilon_j), & j \in G, \\ \text{round}(S_B(x_j) + \epsilon_j), & j \in B, \end{cases} \tag{2.18}$$

where ϵ_j is pseudo-random noise that is normally distributed, with a standard deviation that matches that of the original log image sensor. Responses are rounded, which introduces some quantization noise, because Li *et al.*'s FPN correction preserves the 16-bit integer format of Mahmoodi *et al.*'s image sensor.

2.3.2 Colour Calibration

Colour calibration is performed using the Macbeth chart, a standard colour chart consisting of 24 square patches [29]. Spectral information of each patch is known, along with its XYZ coordinates. Assuming 10×10 pixels per patch, we simulated the stimulus image of the Macbeth chart, the image after FPN correction, and the image after colour correction. This was done using the standard D65 illuminant at $10^4\,\text{cd/m}^2$.

The results of the calibration can be checked qualitatively by converting the true and corrected XYZ values to a displayable sRGB format [39], and then viewing them next to each other. Figure 2.3 illustrates the Macbeth chart, with the left half of each patch showing the corrected values, and the right half the true values. Due to simulated image sensor noise, the left halves exhibit a small pixel to pixel variation that cannot be seen.

To quantify errors, we use the CIELAB colour space due to its approximation of perceptual uniformity [34]. We convert true and corrected XYZ tristimulus values to CIELAB coordinates. Thereafter, the Euclidean distance, between the true and corrected CIELAB vectors, provides an estimate of perceived colour difference. It may be compared to a JND of 2.3 [36]. Although more accurate colour difference formulas exist, the Euclidean distance in CIELAB space was chosen because of its simplicity.

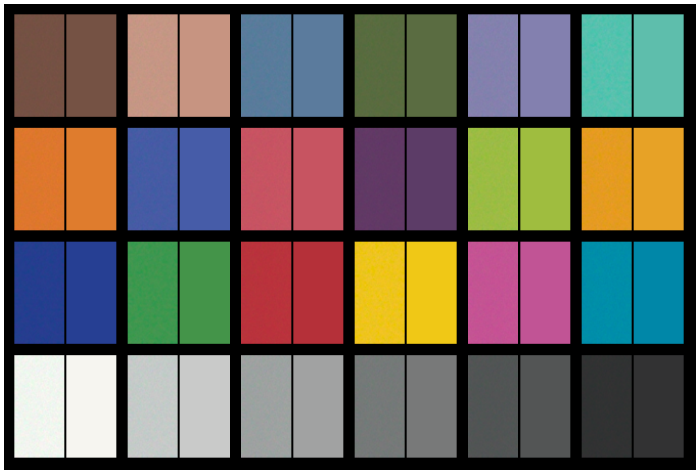

Figure 2.3: True and corrected Macbeth chart in sRGB colour space. The right half of each patch shows the true colour, using the D65 illuminant at $10^4\,\mathrm{cd/m^2}$, while each pixel in the left half shows its corrected colour, which varies imperceptibly due to noise, after calibration and correction.

Table 2.1 gives the median correction error ΔE, over all $24 \times 10 \times 10$ pixels of the Macbeth chart patches, after the calibration and correction. Results for the chosen CFA are given, as well as for an ideal CFA that employs the XYZ spectral functions.

The closer the actual CFA spectral functions are to a linear combination of the ideal spectral functions, the better the results would be, even for linear imaging systems. An improvement of the results when an ideal CFA is used, as indicated in Table 2.1, means that non-idealities of the actual CFA play a limiting factor, irrespective of the nonlinear response of the image sensor.

Figure 2.4 presents a detailed comparison of true and corrected coordinates

Table 2.1: Median CIELAB error of the Macbeth chart image. Using the D65 illuminant, at $10^4\,\mathrm{cd/m^2}$, the median error after colour calibration and correction was calculated. It was done for both system variations, in Fig. 2.1, and an ideal CFA.

Simulated CFA	ΔE (Pre-DM)	ΔE (Post-DM)
Canon 5D	0.8545	1.3860
Ideal XYZ	0.2441	0.3336

in CIELAB space. As six patches in the last row of the Macbeth chart have low a*-b* coordinates, they crowd near the origin of the chromaticity graph. While errors are primarily along the green-red axis, colour matching is good.

Recalling Fig. 2.1, two variations of the imaging system are considered: pre-demosaicking and post-demosaicking. Whereas the colour calibration process is the same for both, the impact of the variations may be analyzed, in CIELAB space after colour correction, using the Macbeth chart. In fact, median correction errors for both variations are reported in Table 2.1. These results imply that pre-demosaicking outperforms post-demosaicking.

Figure 2.5 shows the error after colour correction of the calibration image over a high/wide DR. Although illumination intensity is varied, the colour correction parameters are estimated only once, at $10^4\,\mathrm{cd/m^2}$ as before. In addition to imaging system variations, results are shown for actual and ideal CFAs.

It is evident, in Fig. 2.5, that the pre-demosaicking method outperforms the post-demosaicking method at higher intensities. At lower intensities, however, the reverse is true. In any case, errors are above the JND at lower intensities. While this is partly because of non-idealities of the CFA, it may also be affected by the relatively high dark limit of Mahmoodi *et al.*'s log image sensor [26], a topic that is beyond the scope of this work.

2.3.3 Colour Correction

To validate the proposed method properly, it is important to test colour correction on images that were not used for colour calibration. To this end, the Standard Object Color Spectra (SOCS), published by the International Organization for Standardization (ISO), was used [17]. This database contains reflectance spectra of over 50,000 objects divided into various categories.

The ISO suggests categories of data that are especially suited for evaluating digital cameras. They are called "human faces," "Krinov," which concerns buildings, "flowers," and "leaves." We used all 1,148 spectra, in these 4 categories, and simulated 10×10 pixel patches, as before. We focus on the pre-demosaicking variation of the imaging system, for simplicity, with the ac-

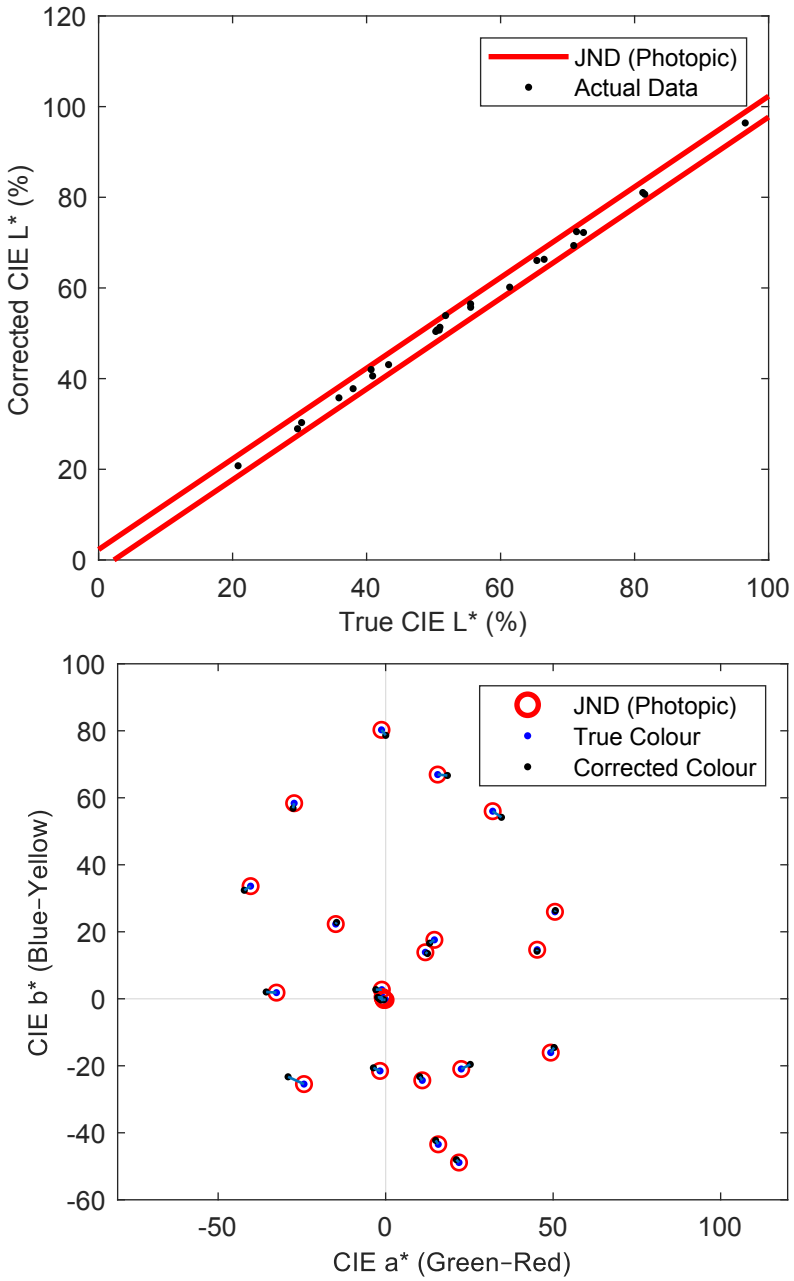

Figure 2.4: Luminance and chromaticity errors of Macbeth chart patches. Red lines and circles in the luminance (top) and chromaticity (bottom) graphs indicate JND regions. Errors are computed after calibration and correction at $10^4\,\mathrm{cd/m^2}$. Each corrected coordinate represents a typical pixel.

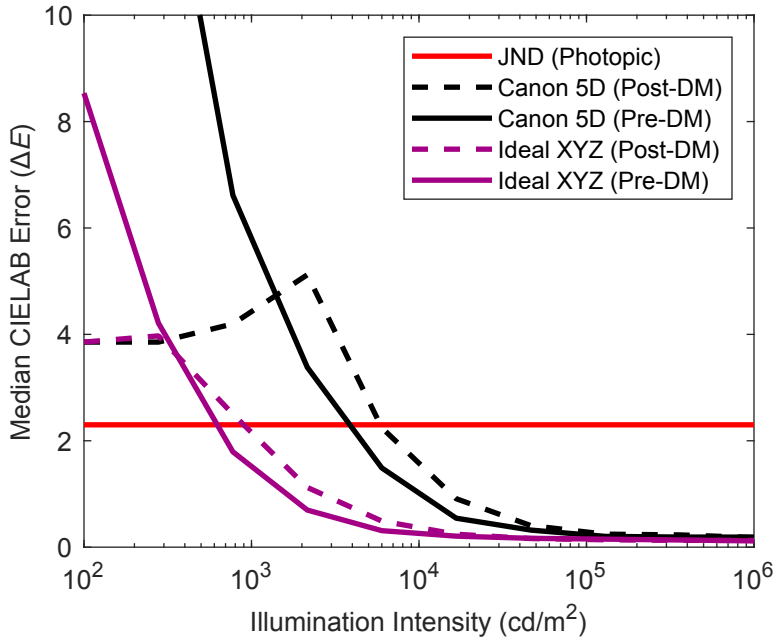

Figure 2.5: Median CIELAB error per intensity of Macbeth chart images. Using the D65 illuminant, after calibration at $10^4\,\mathrm{cd/m^2}$, the median error after colour correction was calculated at various intensities. Results are shown for both system variations, in Fig. 2.1, as well as for an ideal CFA.

tual CFA. Finally, we used the 24 spectra of the Macbeth chart patches, for calibration purposes, and the same D65 illuminant.

Differences, between true and corrected colours, are quantified once again using the Euclidean distance in CIELAB space. Table 2.2 reports the median error of all pixels in each category. Note that each patch has the same number of pixels.

Considering that the JND is 2.3 in CIELAB space, Table 2.2 demonstrates that the colour correction performs well, on median. Given the large number of images per category, compared to the 24 patches of the Macbeth chart, we can estimate a PDF across the images, per category, of the median error per image. Such a result provides a comprehensive assessment of colour correction, because a PDF determines all statistics of interest.

Figure 2.6 shows, for each category, the estimated PDF of the median error per image. The JND is also indicated. Errors vary the most for the flowers category, the only category with a significant error probability mass beyond the

JND, even though the median error is better than that of the faces category.

Because the actual CFA was used in these results, its non-idealities are a limiting factor, as implied previously with Table 2.1. If transmission efficiencies of the red, green, and blue filters, multiplied by the quantum efficiency of the photodiode, were made to closely follow a linear combination of ideal XYZ matching functions, we would expect an improvement in the results.

Figure 2.7 shows the results of correction at varying intensities. As demonstrated, the colour correction proves stable enough for high/wide DR applications involving a large variety of objects. Future work will investigate how to improve performance at dimmer intensities. Possibilities include the improvement of the colour filters and dark limit of the image sensor.

2.4 Conclusion

This chapter proposed a novel method for colour correction of nonlinear CMOS image sensors, which are ideal for high/wide DR applications. The method is neither limited by the specific nonlinear response, i.e., the specific OECF, of the image sensor, nor by FPN, i.e., a variation of the OECF from pixel to pixel due to device mismatch. The only requirement of the method is that the OECF be a monotonic function of light stimulus.

The monotonic property of the OECF allows for cubic Hermite splines to be constructed to allow calibration and correction of red, green, and blue pixel responses. As with linear imaging systems, a 3×3 matrix is also involved.

Table 2.2: Median CIELAB error of simulated SOCS images. The median error after colour correction was calculated using the D65 illuminant at $10^4\,\mathrm{cd/m^2}$, after colour calibration using a Macbeth chart imaged under the same illumination.

Category	Images	ΔE
Faces	538	1.6440
Buildings	370	1.1273
Flowers	148	1.5242
Leaves	92	1.1379

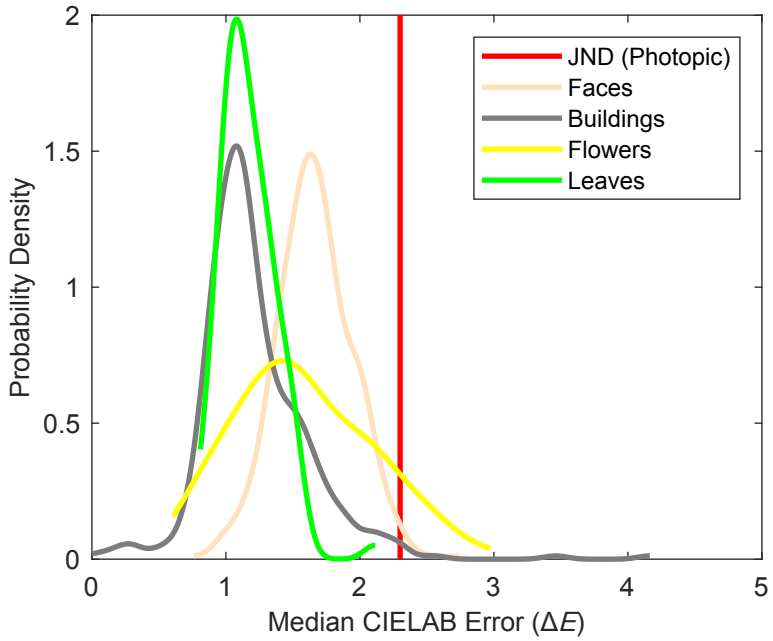

Figure 2.6: The PDF of median CIELAB error of simulated SOCS images. Each SOCS category has enough images to estimate the PDF reasonably well. All correction is performed, using the D65 illuminant at $10^4\,\mathrm{cd/m^2}$, after calibration using a Macbeth chart imaged with the same illumination.

Colour correction is done after FPN correction using Li *et al.*'s method [23], also from our research group. The two methods are complementary and both are needed to realize a colour nonlinear imaging system.

Validation is done by simulating a colour log image sensor using data collected in previous works. This image sensor is used to image a standard Macbeth chart, for colour calibration and its validation, and 1,148 standard objects, for colour correction and its validation. Results show that the proposed method performs well, relative to the JND when errors are measured in CIELAB space, for a large variety of standard objects.

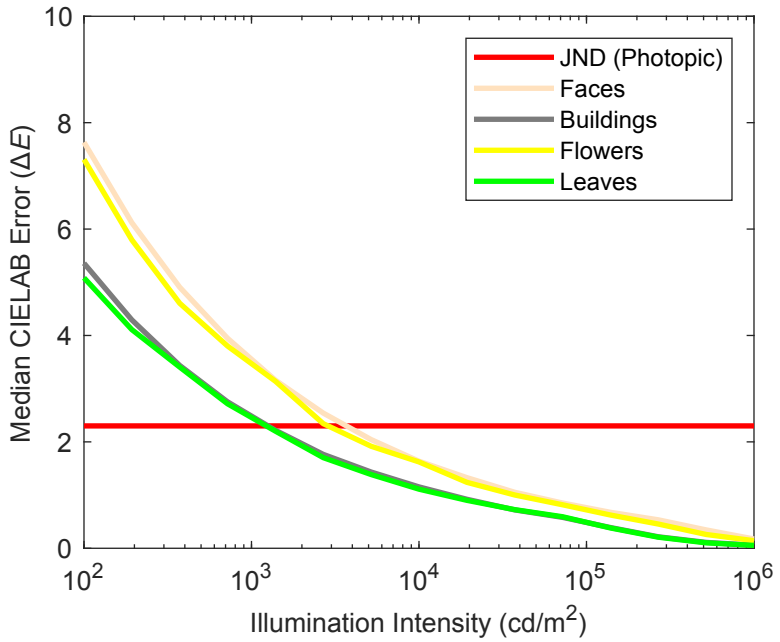

Figure 2.7: Median CIELAB error per intensity of simulated SOCS images. The median error after colour correction, using the D65 illuminant at various intensities, was calculated for each SOCS category, after colour calibration using a Macbeth chart imaged with the same illuminant at $10^4\,\mathrm{cd/m^2}$.

Chapter 3

Nonlinear Demosaicking

In order for nonlinear image sensors to gain a foothold in imaging technology, they must be able to effectively display colour images. While classic demosaicking techniques for linear image sensors are valid for nonlinear image sensors, they are inadequate at handling problems that arise due to the nature of nonlinear image sensors. One such problem is salt-and-pepper noise (SPN). Although SPN is present in linear sensors, nonlinear image sensors behave differently due to SPN and, as such, different techniques need to be implemented to correct this effect. Extending from recent work on SPN filtering, this chapter proposes and evaluates a novel method to demosaick images taken with a Bayer colour filter array (CFA), while simultaneously filtering SPN. The method relies on the use of weighted medians to filter erroneous pixel values while determining a color for each channel at every pixel location. Several variations of the proposed method are considered and evaluated. The Kodak image set is subsampled in a Bayer CFA pattern to produce mosaicked images for testing. SPN is introduced to the image data in varying densities to evaluate performance. Results of the proposed method are compared to those from a popular literature method.

3.1 Introduction

Colour imaging is an integral part of imaging technology. With complementary metal-oxide-semiconductor (CMOS) image sensors (CISs) becoming more prominent, more research is being done on improving results beyond what typ-

ical CISs can produce. In particular, nonlinear CISs are showing promising results, especially in increasing dynamic range (DR) at video rates [1], [26]. While nonlinear CISs have merit on their own, they must ultimately produce colour images in order to be a viable alternative to linear CISs. Currently, the majority of research pertaining to nonlinear CISs does not address the challenges in producing colour images from these types of sensors. A recently published work by Hussain and Joseph [16] shows how to calibrate and correct colour for arbitrary nonlinear colour image sensors.

In order to fully render a colour image using the RGB model, demosaicking has to be performed on the output of the image sensor. Depending on the CFA used, this is typically an interpolation operation that aims to use neighbouring pixel values to determine a value for each of the red, green, and blue channel at every pixel location. Several methods exist in the literature about how to perform this operation. The simplest form of demosaicking is bilinear interpolation, where each colour channel is interpolated independently. This produces significant artifacts as it disregards the high correlation between the RGB channels [27].

Cok implements a method of demosaicking using an inter-channel dependent model, using the idea that the ratio red/green (and blue/green) is constant in the same locality [2]. This idea is not as accurate along edges, where colour gradients can be varying quickly. Kimmel, along with others, have approached the problem of improving performance along edges by performing directional gradients and edge detection to reduce the effect of channel ratios along edges [21], [42]. More recent solutions use deep learning to perform demosaicking. Gharbi *et al.* [12] implement both demosaicking and denoising by training a neural network on a dataset containing images with challenging image features. This method yields improved results, but comes at a cost of increased complexity, requiring more expensive hardware to run in real time.

Malvar *et al.* propose a method of interpolation using simple linear filters that performs well compared to others discussed [27]. In addition to performing well, the method is computationally efficient as it involves simple convolution operations using weighted pixel values. Efficient computation is a

favorable property because it would enable the algorithm to be implemented as low-cost circuitry. Also, the `demosaic` function provided with MATLAB's Image Processing Toolbox implements Malvar *et al.*'s algorithm to demosaick grayscale images, captured with a CFA, into colour images.

Because demosaicking is a self-contained module in the image processing pipeline, its implementation is minimally dependent on how the image is obtained. Demosaicking methods developed for linear image sensors are, in general, applicable to nonlinear image sensors as well. As such, all the techniques mentioned above are relevant for nonlinear image sensors. However, due to their inherent nonlinearity, these image sensors behave differently to phenomena encountered in their linear counterpart. One such phenomenon is SPN. SPN is a type of noise that appears as excessively bright or dark spots in the image due to faulty pixels retaining one value regardless of incoming light. These stuck pixels can be corrected using a static correction method. For example, Tan and Acharya [44] detect and store the locations of such defective pixels to perform SPN correction. With nonlinear image sensors, however, pixels may appear to be stuck at a certain range of luminances but, in fact, may not be defective. In such instances, a dynamic filtering implementation may be preferred to perform SPN correction.

Due to the niche aspects of nonlinear image sensors, not much in current literature can be found about SPN correction for nonlinear CMOS image sensors. Recently, in an award-winning paper, Nascimento *et al.* propose and implement a median filtering approach to remove SPN [31]. They show that, by implementing their method using low-cost field programmable gate arrays (FPGAs), their approach is both effective and efficient in filtering SPN. While their work discusses the complexity of filtering SPN from nonlinear image sensors, it does not discuss how to implement this method for a colour image.

This chapter proposes a new approach which leverages the median operator to simultaneously perform demosaicking and SPN filtering on images taken by an arbitrary image sensor using the Bayer CFA. Relying on the robustness of the median operator against outliers, we extend the work of Nascimento

et al. to use a system of weighted medians to implement demosaicking, while simultaneously removing SPN. Because median filters ignore the effects of outliers, we make the reasonable assumption that, within a local region, there is at most one defective pixel. A significant novelty of the proposed algorithm is that while demosaicking it takes into account that not all of the pixel values might be reliable. Because demosaicking is inherently a spreading operation, one false pixel value can propagate the error over to multiple pixels. By combining SPN filtering and demosaicking into one operation, we prevent the spreading of incorrect information and reduce the blurring of edges.

We first present an overview of the proposed method. Due to the modular nature of the problem, we discuss several variations of the proposed solution, including combining portions of our work with that of Malvar *et al.*'s. Next, we present our results to evaluate our method, and compare its performance with that of Malvar *et al.*'s. Because Malvar *et al.*'s paper compares their method to several others, we find it sufficient to compare our results to theirs. We report PSNR errors in both absolute quantities as well as relative to Malvar *et al.*'s results. Finally, we conclude the chapter by summarizing our work and highlighting its novelty and significance.

3.2 Method and Variations

The basis of the proposed method is that in a set of values, the median of the set is not affected by any outliers in the data. For a finite set of numbers, the median is defined as the middle value that separates the greater half from the lower half of the set. Because extremely high or extremely low values will be pushed to one end of the set, the median can be a good measure of the tendency of a set. Extending the idea of median, we use weighted medians to interpolate missing colour components at every pixel location [9]. A weighted median is defined for an ordered set of numbers $x_1, x_2, ..., x_n$ with positive

weights $w_1, w_2, ..., w_n$, where $\sum_{i=1}^{n} w_i = 1$, as the kth element that satisfies:

$$\sum_{i=1}^{k-1} w_i \leq 1/2, \tag{3.1}$$

$$\sum_{i=k+1}^{n} w_i \leq 1/2. \tag{3.2}$$

In the case where two elements satisfy the above conditions, a new element with a value equal to the mean of the two elements can be created, and assigned a weight of zero. Assuming all the weights are rational, it is always possible to represent the weights $w_1, w_2, ..., w_n$ such that they are all positive integers $W_1, W_2, ..., W_n$, where

$$w_i = \frac{W_i}{W_1 + W_2 + ... + W_n}. \tag{3.3}$$

In this case, the weighted median can be understood as the unweighted median of the set of numbers where each element x_k is repeated W_k times.

For the purpose of our method, we require integer weights and, in particular, *small* integer weights, because we would ultimately like to extend this work to an FPGA implementation based on the designs of Nascimento *et al.* In accordance with their philosophy of achieving a fast and efficient algorithm, we want small integer weights, W_i, to reduce the amount of logic and memory required to implement the demosaicking with circuits. Nevertheless, a non-uniform weighting approach is useful in demosaicking because it allows for certain pixels to contribute more towards the median than other pixels.

In order to perform the SPN filtering and demosaicking, we first segment the image into its three separate colour channels based on the Bayer CFA. Initially, each channel is treated separately. We define local windows over which to perform the weighted medians. These windows are displayed in Fig. 3.1. Determining green pixel values requires the smallest window size of 3×3 pixels due to the green channel being sampled at twice the rate of the red and blue channels. For green at red or blue locations, we use equally weighted medians because the Bayer CFA ensures that each red or blue pixel is surrounded by four green pixels.

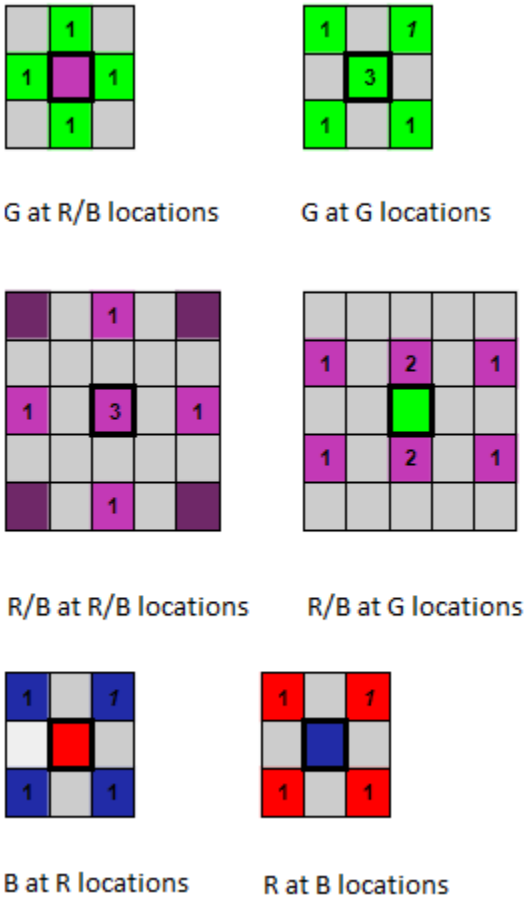

Figure 3.1: Summary of masks to perform nonlinear demosaicking. The pixel with the dark borders is the pixel being evaluated. Only relevant pixels are numbered in each window. The number on a relevant pixel shows the weight assigned to the pixel.

Unlike other demosaicking methods, we have an additional step where we determine a green value for a pixel already containing a supposed "true" green value. This is due to the underlying assumption of SPN filtering that every pixel is at risk of being defective. Because each surrounding green pixel considered is equidistant from the central pixel, they are all weighted equally. However, Fig. 3.1 shows that the mask assigns a weight three times that of the surrounding pixels to the center pixel. This is done to reduce the amount of blurring, while still being able to filter an outlier. As mentioned earlier, we make the assumption that within our local region, at most one pixel is defective. If the center pixel happens to be a non-defective pixel, its value will

contribute more to the median than all the others. If the pixel happens to be defective, however, then a weight of three ensures that it will not dominate the median and the resulting final value of the pixel will be one of the four surrounding non-defective pixels.

Determining pixel values for the red and blue channels requires increasing the window size to a 5×5 pixel region. From Fig. 3.1, we can see that determining red at red locations, or blue at blue locations, uses the full window, including the four nearest pixels of the same colour. Similar to before, this step weights the central pixel at three times the weight of the four surrounding pixels. Red or blue at green locations requires two masks because each green appears either in the same rows or the same columns as the red or the blues. Because the masks are rotations of each other, only one case is shown. Following similar logic as before, the two pixels closer to the central pixel are weighted more to reduce blurring, while still performing SPN filtering. Lastly, red at blue locations, and blue at red locations, are treated the same way because the geometry is the same. Equally weighted medians are used because of the equal distances between the surrounding pixels and the central pixel.

The method described thus far will be referred to as nonlinear demosaicking 1 (NLD1). At this point, it performs SPN filtering well, but it does not consider any inter-channel dependencies. This leads to lower performance than desired in demosaicking. An improvement on this method is to perform NLD1 on the the green channel only and then define:

$$R' = R - G, \tag{3.4}$$

$$B' = B - G, \tag{3.5}$$

where G is the demosaicked green channel. We then perform NLD1 on the red and blue channels only, as represented by R' and B', respectively. Finally, the demosaicked green channel is added back to the demosaicked red and blue channels, restoring R and B from R' and B', respectively. This improved method is referred to as nonlinear demosaicking 2 (NLD2).

As mentioned previously, techniques developed for linear image sensors can be applied to images taken by nonlinear image sensors. Therefore, if SPN

filtering is considered separately, Malvar *et al.*'s method can be applied to images taken by nonlinear image sensors. Consequently, a third variation of the proposed method is to use some of the masks described above to only perform SPN filtering on the separate channels, and implement desmosaicking using Malvar *et al.*'s method. We refer to this method as SPN filtering 1 plus linear demosaicking (SPNF1+LD). A final variation we discuss is to modify the SPNF1+LD method to use uniform weights in the SPN filter for determining medians. This is similar to the SPN filter used by Nascimento *et al.*, notwithstanding our extensions for colour image sensors. We refer to this method as SPN filtering 2 plus linear demosaicking (SPNF2+LD).

3.3 Results and Discussion

This section evaluates the proposed method and its variations. We use the Kodak set of true colour images that is used by Malvar *et al.* [27], Kimmel [21] and Wang *et al.* [42], as well as others, to evaluate demosaicking algorithms. The Kodak true colour images are a set of 24 images of size 512×768 pixels each, with each pixel represented using 24 bits. We subsample the Kodak images according to the Bayer CFA to produce the mosaicked red, green, and blue channels for each image. We show absolute PSNR error relative to ground truth, as well as results relative to Malvar *et al.*'s method. We present results of tests where we vary the amount of SPN while measuring error. We also present a table with our PSNR errors, broken down by colour channel, at a typical SPN density.

The proposed method attempts to solve the problem of demosaicking when the image contains SPN. We introduce SPN to the test images using the `imnoise` function provided with MATLAB's Image Processing Toolbox. This function allows us to vary the density of SPN. Using the density parameter, the `imnoise` function sets certain pixels in the image to zero, and others to the maximum value of the image type, which for our data is 255. We evaluate our method by running our algorithm on the first 15 images of the Kodak image set. We use the first 15 images to be consistent with Malvar *et al.*'s published

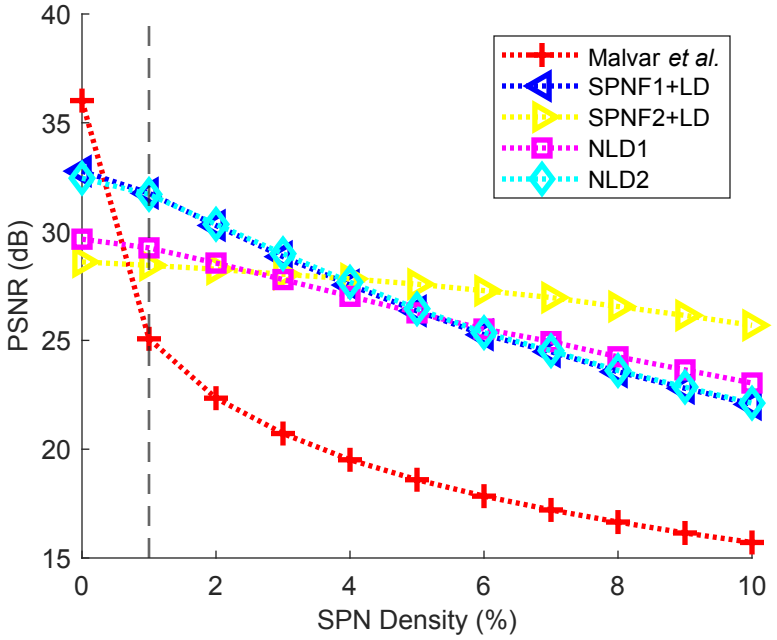

Figure 3.2: Absolute PSNR error relative to ground truth. As SPN density increases, Malvar *et al.*'s method's PSNR falls quickly. For high SPN the overall quality of the image decreases substantially.

results.

After the various methods have been implemented,we determine the root-mean-square error (RMSE) between the resulting image and the ground truth from the Kodak image set. We present our results in the form of PSNR, so they may be compared to Malvar *et al.*'s published results. The PSNR is determined using the following equation:

$$PSNR = 20 \log \left(\frac{255}{RMSE} \right). \tag{3.6}$$

From Fig. 3.2, we can see firstly that Malvar *et al.*'s method's performance drops immediately after SPN is introduced. This is a result of the demosaicking process propagating erroneous pixel values. We are primarily interested in the region under 5% SPN density. Higher SPN densities are of less interest to us because the image quality becomes significantly lower. As expected, NLD1 does not perform as well as NLD2 in the area of interest to us. We see that SPNF2+LD performs better than SPNF1+LD in the higher SPN density region, but worse in the lower density region. This is an expected

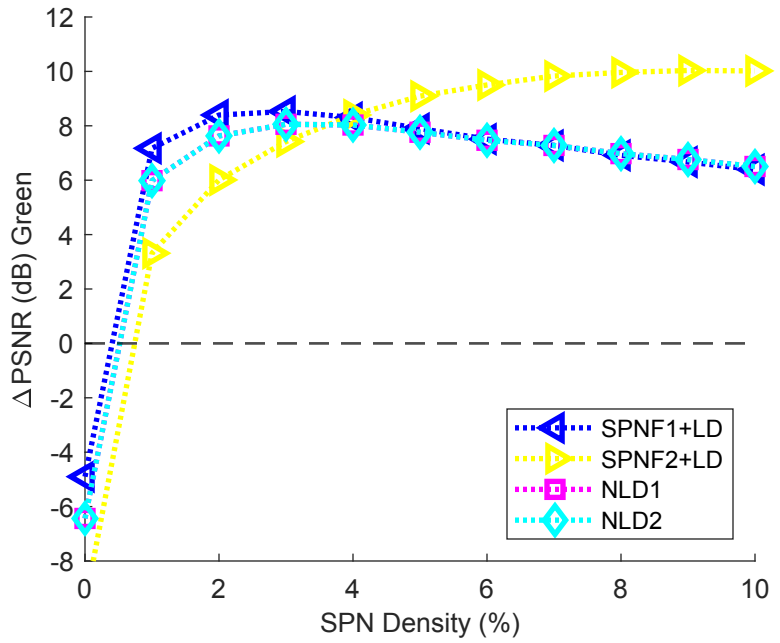

Figure 3.3: Mean error relative to Malvar *et al.* in the green channel. Relative to Malvar *et al.*'s method, SPNF1+LD performs well in the green channel. We expect NLD1 and NLD2 to be identical in the green channel.

result because, with low SPN, equally weighted medians will increase blurring as neighbouring pixels are favoured equally to the center pixel. However, when SPN is present in larger amounts, SPNF2+LD performs better because it is robust against at most two defective pixels in the window. This property is a consequence of using uniform weights in the SPN filtering masks. When taking the median of five pixels, *more than* two pixels would have to be erroneous for the median to be an erroneous value. While being robust to two erroneous pixel values is a desirable property, it comes at a cost of increased blurring. Because we focus on lower SPN densities, it is evident that the weighted median approach is more useful. Of relevance, the peak signal-to-noise ratio (PSNR) of SPNF1+LD is equally high in this region.

We can also examine the individual colour channels to see how the errors are distributed. These results are shown, in Figs. 3.3 and 3.4, relative to Malvar *et al.*'s method. Results greater than zero indicate a surpassing of Malvar *et al.*'s method. We expect to see identical results, in the green channel, for NLD1 and NLD2 because the only difference between the two methods is the

Table 3.1: Our results relative to Malvar *et al.* at 1% SPN density. The four variations of the preferred NLD2 method are performed on the first 15 images of the Kodak image set. The results are given relative to Malvar *et al.*'s results.

	SPNF1+LD			SPNF2+LD			NLD1			NLD2		
	R	G	B	R	G	B	R	G	B	R	G	B
1	3.4	3.1	3.5	0.3	-0.7	0.5	-0.3	2.1	-0.4	3.7	2.1	3.9
2	7.1	9.5	8.9	4.8	6.3	6.7	5.1	8.7	6.6	7.6	8.7	9.5
3	9.7	10.7	9.8	6.8	7.1	7.3	7.3	9.7	7.0	10.3	9.7	10.3
4	8.2	10.5	9.2	5.0	6.6	5.9	5.6	9.0	6.4	8.4	9.0	9.7
5	3.7	4.6	4.1	-0.3	0.0	0.0	0.4	2.9	0.3	4.5	2.9	4.5
6	4.8	4.8	4.9	1.2	0.6	1.5	1.2	3.7	1.1	5.1	3.7	5.0
7	9.0	10.3	9.2	6.0	6.7	6.3	6.1	8.9	5.9	9.8	8.9	9.9
8	2.3	1.5	2.1	-0.7	-2.2	-0.8	-1.7	0.8	-1.9	2.9	0.8	2.7
9	8.5	9.3	8.6	5.8	5.6	5.9	5.1	8.2	5.2	9.3	8.2	9.2
10	8.2	9.2	8.1	4.7	5.0	4.6	4.9	8.0	4.7	9.0	8.0	8.7
11	5.6	6.2	6.0	2.5	2.2	2.9	2.5	4.9	2.6	6.1	4.9	6.3
12	9.0	10.0	9.0	6.6	6.7	6.6	6.2	9.1	5.6	9.7	9.1	9.6
13	1.6	1.5	1.7	-2.2	-3.0	-2.1	-1.6	-0.2	-1.6	1.7	-0.2	1.6
14	5.3	6.5	6.0	1.9	2.2	2.6	2.4	5.1	2.5	6.0	5.1	6.3
15	7.7	10.0	8.5	5.6	6.7	6.4	5.7	8.9	5.3	8.5	8.9	9.3

calculation for the red and blue channels. Similar to what was observed in Fig. 3.2, SPNF2+LD continues to do relatively well at higher SPN densities, but due to the high SPN density, the resulting image has a significantly lower quality. We can see, in Figure. 3.4, that NLD2 surpasses all other methods, in the red and blue channels, at low SPN levels. At the lowest SPN densities, NLD1 performs almost identically to SPNF2+LD.

Additionally, Tab 3.1 presents results for the various methods at an SPN density of 1%. 1% is chosen as a reference SPN density because it is low enough to produce quality images but high enough to show that a traditional demosaicking method is insufficient. The table, similar to one presented by Malvar *et al.*, shows the performance of all the described methods at 1% SPN density, relative to Malvar *et al.*'s results.

Finally, PSNR is not a complete measure of demosaicking. It is important to look at the images to determine performance. From the set of images, we selected an image and a region with high frequency components, as that is where errors tend to occur. Figure 3.5 shows a visual comparison of the differ-

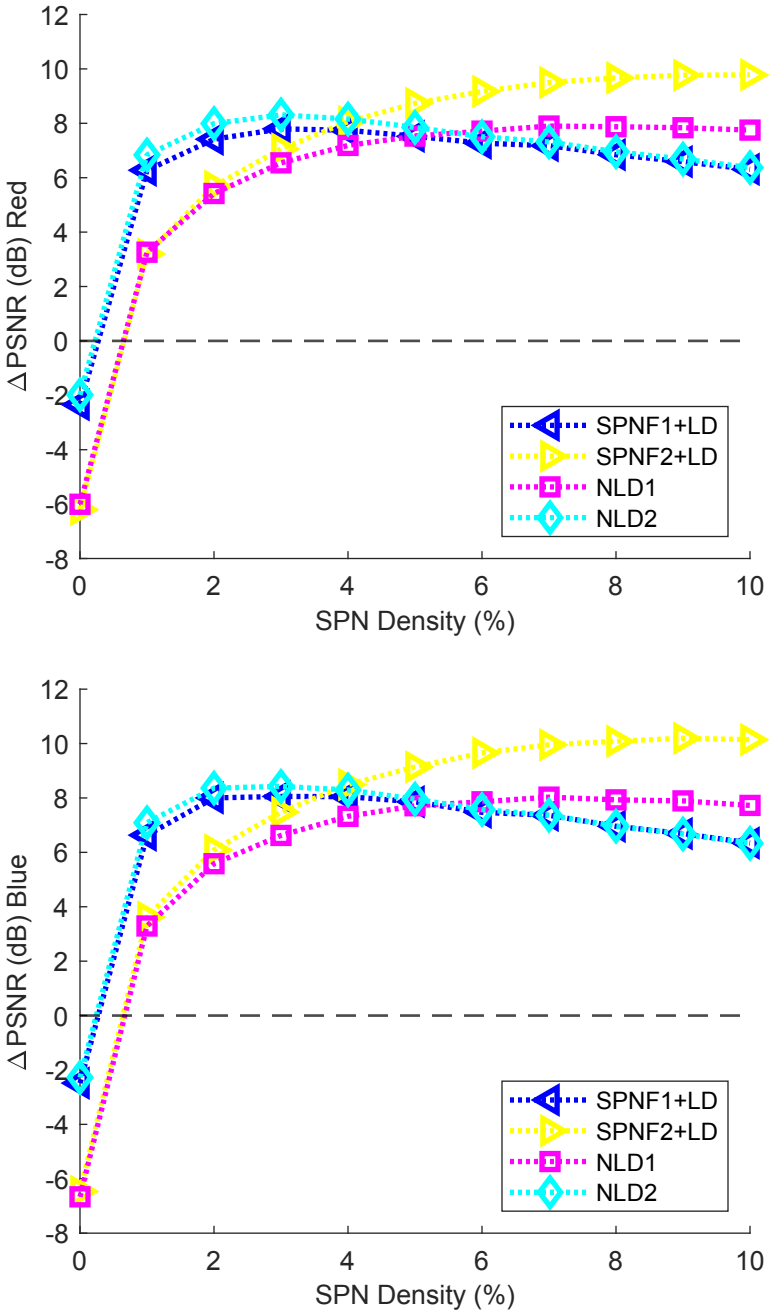

Figure 3.4: Mean error relative to Malvar *et al.* in red and blue channels. NLD2 outperforms all the other methods at low SPN densities. In addition, both NLD2 and SPNF1+LD surpass Malvar *et al.*'s method almost immediately.

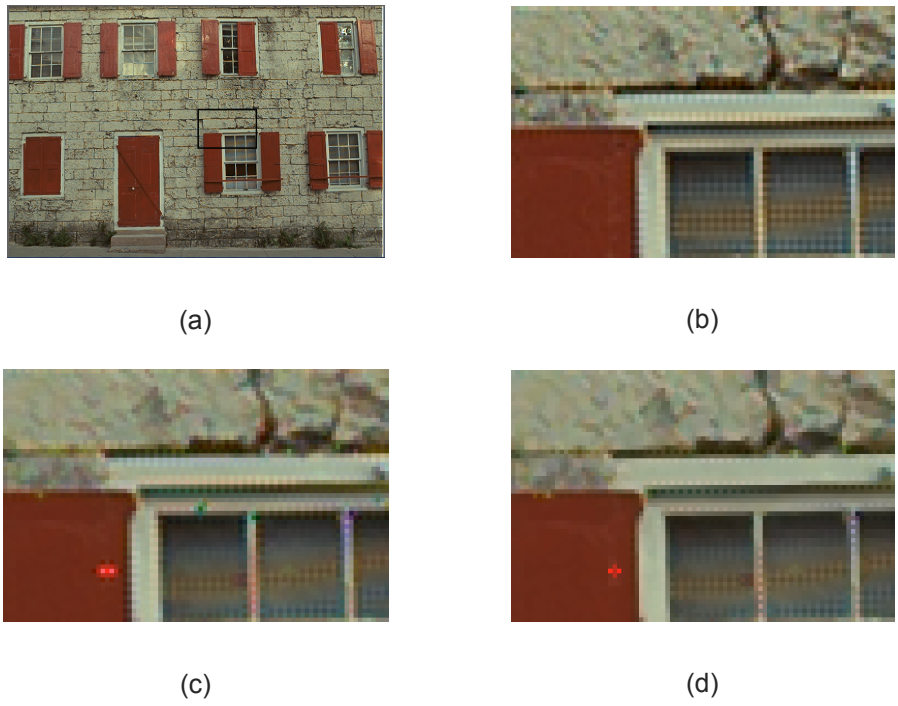

Figure 3.5: Comparison of demosaicking using different methods. (a) Original image from the Kodak dataset. (b) Result of Malvar *et al.*'s algorithm in a high frequency region at 0% SPN density. (c) Result of SPNF1+LD in the same region at 1% SPN density. (d) Result of NLD2 in the same region at 1% SPN density. NLD2 shows the clearest results, and also filters SPN the most effectively.

ent techniques. The first image is the true colour image from the Kodak image set, with a box around a region of interest. The second image is the region of interest desmosaicked using Malvar *et al.*'s method at 0% SPN density. Because we have already shown that Malvar *et al.*'s method is not suitable with SPN included, we only focus on the quality of its demosaicking. The third and fourth images show the result of SPNF1+LD and NLD2, respectively, at 1% SPN density. Comparing Fig 3.5(c) to Fig 3.5(d), it is evident that SPNF1+LD is not as effective along edges as NLD2. We also note Fig 3.5(c) depicts significantly more remnants of SPN, compared to Fig 3.5(d). As a final note, we can see that although Fig 3.5(d) filtered SPN, there is not a stark difference in quality between (d) and (b), which filtered no SPN.

From the results shown above, we can conclude that the most robust

method to perform both demosaicking and SPN filtering is NLD2. We are primarily interested in low SPN densities, as our model explicitly relies on defective pixels being isolated outliers in very small neighbourhoods.

3.4 Conclusion

Due to increasing interest in the benefits of nonlinear image sensors, it is important to consider how previously defined techniques for performing image signal processing are affected. One essential process that is required to produce a colour image is demosaicking. With the addition of SPN in nonlinear image sensors, demosaicking methods for linear image sensors need to be revised. This chapter developed a novel approach to perform demosaicking while simultaneously performing SPN correction. We showed multiple variations of the proposed method, including ones that incorporated Malvar *et al.*'s method. This algorithm, which is implemented by MATLAB's `demosaic` function, was actually developed for linear image sensors. We show that, while it produces good results at 0% SPN density, performance of this algorithm drops once SPN is introduced.

As SPN is a phenomenon that is encountered in nonlinear image sensors, it is necessary to revise traditional methods of demosaicking. Consequently, we developed various methods and concluded that NLD2 outperformed all other methods, maintaining a high PSNR when SPN was present in reasonable quantities. NLD2 is the combination of applying weighted median filters and considering inter-channel dependencies. It builds on NLD1 by performing NLD1 first on the green channel, and then on the difference between the green and red channel, and the green and blue channel. The green channel component is added back to create the final result. This extra consideration shows results superior to all other methods considered. We showed that classic methods for linear image sensors were not suitable if SPN was present in even small quantities. Lastly we looked at visual examples of how our proposed method was robust against SPN and performed demosaicking at a standard comparable to classic methods for linear image sensors.

Chapter 4

Conclusion

Due to the limited dynamic range (DR) provided by linear complementary metal-oxide-semiconductor (CMOS) image sensors, nonlinear image sensors have started to become more relevant. These image sensors allow high/wide dynamic range (HDR) images to be captured at video rates and have been the subject of ongoing research. Colour is an essential aspect of visible-band imaging. Colour algorithms developed for linear image sensors are not designed for nonlinear image sensors. As such, new algorithms need to be investigated. This chapter summarizes the two novel methods proposed in this thesis. A colour correction algorithm for monotonic nonlinear CMOS image sensors was developed, which uses a combination of linear and nonlinear techniques to perform colour correction. A nonlinear demosaicking algorithm was also developed, which performs demosaicking on an image captured with a Bayer colour filter array (CFA) while simultaneously filtering salt-and-pepper noise (SPN). Future works for this thesis are also presented. A fixed-point design of the proposed algorithms would allow for real-time processing of images with an FPGA implementation. A 3D printed camera body would allow for the device to be portable, which can enable the collection of experimental results outside lab of environments.

4.1 Summary and Contributions

Although there has been research done on improving noise in logarithmic (log) and linear-logarithmic (linlog) image sensors, colour algorithms for nonlinear

image sensors need to be investigated. Traditional techniques are not designed to perform colour operations on images captured by nonlinear image sensors. This thesis makes two contributions to the development of colour algorithms for nonlinear image sensors. In Section 4.1.2, we review the colour correction algorithm for nonlinear monotonic image sensors from Chapter 2, and highlight its novelty and significance. In Section 4.1.3, we present a summary of the nonlinear demosaicking algorithm developed in Chapter 3, along with the contributions made to knowledge.

4.1.1 Motivation and Background

As the Senior Vice President of Sony, Tomoyuki Suzuki [40], said at the 2010 ISSCC, the next goal of CMOS image sensors is to outperform the human visual system. In this effort, one significant bottleneck is the limited DR that most linear CMOS image sensors have. With the aim to increase the DR of imaging systems, significant research has been done on using nonlinear image sensors. In particular, log and linlog image sensors have come out as promising solutions. These image sensors are able to dramatically increase the DR of the imaging system because they do not respond linearly to incoming light. Their nonlinear response allows them to remain unsaturated at over a higher range of luminances than linear image sensors. Various log and linlog image sensors have been developed that report DRs greater than 120 dB [8], [24].

Advances in CMOS image sensor technology have had significant benefits in a wide variety of industries. In the medical imaging field, CMOS X-ray imagers have been developed, including HDR ones, that show improved performance over traditional amorphous silicon (a-Si) flat panel detectors [11]. Improving on monochromatic X-ray imaging, techniques to colourize X-ray images have also been developed [32]. The introduction of colour allows for more information about the scene to be retained. Autonomous vehicle applications are a natural application of visible-band HDR imaging. Because there is a large range of luminances encountered when driving, it is essential that cameras remain unsaturated to provide continuous information to the algorithms governing the operation of the vehicle. HDR image sensors are

capable of handling a high/wide DR of luminances without saturation of pixel responses.

Although nonlinear image sensors have numerous benefits over linear image sensors, there are some challenges that need to be addressed. Because nonlinear image sensors behave differently from linear image sensors when encountering the same stimulus, image signal processing techniques for linear image sensors need to be refined to meet the needs of nonlinear image sensors. In particular, colour algorithms need to be revised to make them more suitable for processing images captured by nonlinear image sensors. Linear colour correction involves transforming data from a device-dependent camera space to a standard colour space using a matrix transform. This technique is not sufficient for nonlinear image sensors [19]. Moreover, traditional demosaicking algorithms, which are necessary to render full colour images, can propagate erroneous pixel values caused by SPN, which behaves differently in nonlinear image sensors than it does for linear image sensors [31].

This thesis developed a novel colour correction algorithm for nonlinear image sensors. The proposed algorithm, consisting of both a linear and nonlinear colour correction stage, was validated using a simulation-based approach, and showed results below the just noticeable difference (JND) threshold for a wide variety of colour patches. Additionally, this thesis also presented a nonlinear demosaicking algorithm for images captured with a Bayer CFA that was able to, in the presence of SPN, outperform a leading technique mentioned in the literature.

4.1.2 Colour Correction

Colour is an integral component of visible-band imaging. Therefore, methods on colour correction for nonlinear image sensors need to be addressed. In recent works involving nonlinear sensors, colour is not directly mentioned. Methods have been developed that alter the log and linlog image sensor to improve performance at darker luminances [1], [3]. A prominent feature of many works on nonlinear image sensors is that they pertain to a specific sensor response ,i.e., log or linlog. Using a mathematical model to describe the behaviour of

a log image sensor [18], methods have been developed to correct fixed pattern noise (FPN) for the class of log image sensors [15], [19]. While these methods perform well, they are not applicable to models that differ from the traditional log model.

The motivation for this work was to develop and evaluate a method that is capable of integrating colour into images taken by arbitrary nonlinear image sensors. Therefore, the method presented in this thesis is applicable to a wide variety of image sensors, as it does not make major assumptions about what the response of the image sensor will be. This method is built on Li *et al.*'s work on using low-degree polynomials and cubic Hermite splines for FPN and photometric correction [23]. Relying only on the monotonicity of the pixel response, Li *et al.*'s method was tested with data from a log sensor and showed that FPN correction using the generic method was competitive with FPN correction using the log model [23]. The restriction of monotonic image sensors is reasonable, as monotonicity is a typical feature for many image sensors.

Extending on this work, this thesis presented a novel method to perform colour correction on images taken by arbitrary monotonic image sensors. The proposed method is composed of two stages: a calibration stage that is required to establish parameters; and a correction stage that performs colour correction on all frames captured by the image sensor. Correction is done by using a combination of linear and nonlinear techniques. The proposed colour correction method is intended to be implemented as a subsystem in an image processing pipeline. In order for a full colour image to be displayed, the image must be demosaicked to generate a tristimulus value of red, green, and blue at every pixel. For this method, we used Malvar *et al.*'s algorithm [27], which is implemented by MATLAB's `demosaic` function.

Prior to colour correction, this method assumes that FPN correction is performed using Li *et al.*'s method [23]. Li *et al.*'s method is calibrated by taking pictures of a uniform background under varying luminances. In this thesis, this calibration process is extended to the colour scenario by segmenting pixels into red, green, and blue sets, and constructing a separate cubic Hermite

spline for each set. Linear correction is performed by determining a 3×3 matrix that would convert the tristimulus value from the camera space to a standard colour space such as CIE XYZ. This is a standard technique in colour correction, so the novelty in this portion is not in the transformation itself, but rather in how the matrix is determined.

Using data gathered from a standard colour chart, e.g., the Macbeth colour chart, we capture images under varying intensities of a known illuminant, e.g., the D65 illuminant. The true CIE XYZ values of the colour chart are known. Using a sum of square errors (SSE) method, we can quantify the error between the captured images and the "true" images. This error can then be minimized using a standard optimization algorithm to determine the optimal transformation matrix. Once calibration is completed, correction can be implemented for every pixel in each captured frame.

Validation of the method using experimental data is difficult because a nonlinear image sensor with a standard CFA is not readily available. As such, we tested our design using a simulation approach. A nonlinear image sensor was modelled using data collected from Mahmoodi *et al.*'s log sensor [26]. The algorithm was calibrated using the Macbeth colour chart [29] and demosaicking was done using Malvar *et al.*'s method.

Results of the validation are given as the median 1976 CIE L*a*b* error of all the pixels. We showed the results of our method on data taken from a standard collection of object reflectances [17], using illuminant D65 at $10^4\,\mathrm{cd/m^2}$. Testing on the recommended categories, we showed that most of the correction was accurate to below the JND of 2.3 [36]. We also showed the results of varying illuminant intensities on colour correction. The results of our experiment concluded that the method proposed works well, especially at higher intensities, where colour errors were well below the JND.

A prominent feature of the proposed method is that it places minimal restrictions on the type of image sensors it can be applied to. While others have presented colour correction techniques tailored for specific classes of image sensors [15], [19], this method is applicable to all nonlinear monotonic image sensors. Despite the generic approach, the method performs very well under

testing conditions.

4.1.3 Nonlinear Demosaicking

In addition to colour correction, demosaicking is another process that is required before a final colour image can be obtained. In order to display a colour image, a tristimulus value of red, green, and blue must be determined for every pixel location. This often requires an interpolation technique, as most image sensors use a CFA to filter incoming light. Depending on the CFA used, there are many techniques discussed in the literature to perform demosaicking.

Edges are a challenging problem for demosaicking algorithms, because they contain high frequency data. Colour gradients can be varying quickly across, edges whereas they are more gradual within local objects. Techniques have been developed that perform directional gradients and edge detection to improve performance along edges [21], [42]. Malvar *et al.* propose a method of demosaicking using linear filters and convolution operations [27]. This method is adopted by MATLAB in their `demosaic` function, as part of their Image Processing Toolbox.

Demosaicking is largely a self-contained operation, in that there is minimal dependency on other aspects of the image processing pipeline. As such, many demosaicking methods developed for linear image sensors are applicable to nonlinear image sensors as well. However, nonlinear image sensors, by design, behave differently than linear image sensors when encountering the same phenomenon. One such difference is in the presence of SPN. SPN is a type of noise that appears as excessively bright or dark spots in the image, due to pixels being "stuck". Static SPN correction methods can store the location of such pixels and perform correction on the affected pixels [44]. For nonlinear image sensors, however, SPN can gain a dynamic component, where pixels appear to be "stuck" at certain luminances, but active at different luminances [31]. In this case, a dynamic filtering method can be used.

In a recent award-winning paper, Nascimento *et al.* designed and implemented a technique for filtering SPN in real time [31]. While this work shows a promising solution to SPN filtering for nonlinear image sensors, it does not

discuss SPN filtering for a colour image. In this thesis, we proposed and evaluated a method of performing demosaicking and SPN filtering simultaneously for nonlinear image sensors. Extending the work of Nascimento *et al.*, we use a system of weighted medians to perform demosaicking on images containing SPN. Because medians are robust against outliers, we make the assumption that within a local region, there is at most one defective pixel. This is a reasonable assumption, as most pixels in a pixel array are assumed to be operating correctly.

In order to perform the SPN filtering and demosaicking, we first define a set of weights which we apply to a local window. This window is kept as small as possible to decrease blurring in the image. The weighted medians are applied according to the colour channel being demosaicked, and a tristimulus value for each pixel is determined. To account for the inter-channel dependencies, the green channel is handled first. The weighted medians are then applied to the difference between the red and green channel, as well as the blue and green channel, rather than just the red and blue channels. The final red and blue results are obtained by adding the green channel back. Because linear demosaicking techniques are valid for nonlinear image sensors as well, we also consider using Malvar *et al.*'s method along with our SPN filtering method to see which method yields the better results.

Validation of this work is done by comparing our results to that of Malvar *et al.*'s. Like Malvar *et al.* and others, we use the Kodak image set to test our method. We present our results as peak signal-to-noise ratio (PSNR) relative to ground truth, and relative to Malvar *et al.*'s results. By introducing SPN to the Kodak image set, we show that while Malvar *et al.*'s method achieves a high PSNR at 0% SPN, the performance of the algorithm decreases significantly as SPN is introduced. We limit our focus to the region of SPN below 5% as, beyond that, the quality of the images is significantly lower.

We also present a mean error, relative to Malvar *et al.*'s results, across multiple images for each of the red, green, and blue channels. In addition, similar to Malvar *et al.*, we present a table of results at 1% SPN density to show the relative performance of each proposed method. Finally, we present a visual

result that illustrates the results of demosaicking along edges. Our results conclude that our proposed method successfully filters SPN while performing demosaicking. For SPN densities below 5%, we show that our method achieves a high PSNR, along with good visual results along edges.

4.2 Future Work

In this thesis, two colour algorithms for nonlinear CMOS image sensors were presented. First, a colour correction algorithm for arbitrary monotonic nonlinear CMOS image sensors was developed. The algorithm consisted of a nonlinear, as well as a linear, component to address the nonlinear nature of the sensor response. Additionally, an algorithm for demosaicking was presented, which was able to simultaneously filter SPN present in nonlinear CMOS image sensors. This work can be extended in various directions. One immediate extension is to join the two operations presented into one operation which combines the properties of the two algorithms. Additionally, a fixed-point design for the joint colour correction and nonlinear demosaicking algorithm can be developed, which is more efficient for an FPGA implementation. To facilitate gathering of experimental data, a 3D printed camera body can be constructed to house the image sensor and necessary peripherals, allowing the camera to be taken out of a laboratory environment.

4.2.1 Fixed-Point Implementation

The methods presented in this thesis were developed in MATLAB, which is a high-level computing language. It uses floating-point numbers, meaning the location of the decimal is not fixed. This, in general, allows for more accurate calculations and a larger range of possible numbers. The drawback to floating-point operations is that they are slower, and more computationally expensive, than fixed-point operations. In an FPGA implementation, where efficiency and low-power are desirable, a fixed-point implementation is preferred. However, using fixed-point operations may introduce errors due to the fixed number of bits for the integer and fractional parts of the number. By varying the binary

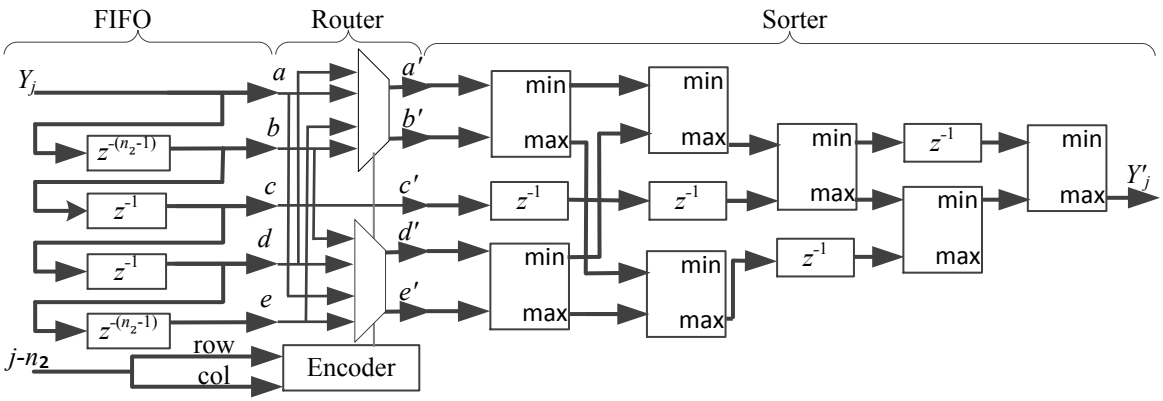

Figure 4.1: An SPN filter implemented with digital circuits. This design can be extended to implement our algorithm. Taken from Nascimento *et al.* [31].

point position and the total wordlength used, the error can be minimized.

During the colour correction calibration process, a 3×3 transformation matrix is determined. The elements of this matrix need to be converted to a fixed-point representation. For an accurate conversion, we would like to use a large number of bits for the wordlengths t_k, where $1 \leq k \leq 9$. However, we also want to minimize t_k so as to use the least amount of memory and power when performing operations. Similar to how the transformation matrix was determined, the optimal parameters can be determined by defining a function, which depends on the parameters t_k, that computes the SSE between the floating-point and the fixed-point representations. Finding a minimum of this function would result in the optimal wordlengths.

A fixed-point implementation for Malvar *et al.*'s algorithm would require a conversion of the mask weights that are used to perform the demosaicking. However, in our nonlinear demosaicking algorithm, the mask weights are not multiplicative. Rather, the weights are a measure of how many times the pixel is used in the median calculation. As such, the only operation that needs to be performed by the FPGA circuits is the median operation, rather than the convolution operation used in Malvar *et al.*'s algorithm.

Nascimento *et al.* developed an SPN filter for an FPGA implementation, as shown in Fig 4.1. This work can be modified to implement our algorithm by introducing a method to repeat certain pixel values depending on the weight

Figure 4.2: Prototype of camera body. A prototype of a camera body designed in TinkerCad and 3D printed. The dimensions are set for a typical microcontroller board stacked with an FPGA board. An LCD screen is hooked onto the body of the camera to view images in real time.

associated with the pixel. In addition, the colour channels would have to be segmented according to the Bayer CFA. Segmenting the colour channels would require handling each colour channel separately, which is convenient because FPGAs can perform parallel computation, rather than just sequential. This parallel processing would allow for faster operation of the algorithm.

4.2.2 Experimental Results

As mentioned previously, obtaining experimental data from nonlinear CMOS image sensors is difficult because colour nonlinear cameras are not readily available. A possible extension of this work is to develop methods that can allow nonlinear image sensors to obtain colour experimental results outside of lab environments. With the advent of maker culture, 3D printing is a promising tool that may allow technologies previously limited to lab environments to enter an unthethered experimental stage of performance evaluation.

Using a high-level computing language like MATLAB, this work shows a preliminary proof of concept. With an FPGA implementation, along with a suitable image sensor and colour filters, the work can be extended to be a functional prototype of a colour nonlinear camera. However, in order to obtain diverse experimental results, the prototype must be portable enough to be taken out of the laboratory. For this purpose, a camera body that houses the image sensor, the FPGA, and all other necessary peripherals can be constructed. The camera body should be able to protect all the electronic hardware from outside elements, but still allow access to the hardware if required.

Figure 4.2 shows a prototype of a camera body that was designed to house a Beaglebone board, along with an FPGA board stacked on top, in addition to the image sensor. A piece to allow the lens to be attached was affixed in front of a hole in the camera body to allow focused light to reach an image sensor. A folding compartment containing an LCD screen was also attached to the camera body, allowing the capturing and viewing mechanisms to be contained in the same body.

Red, green, and blue colour filters may be purchased and screwed onto the lens. This provides a simple way to produce colour experimental results. After taking three pictures, selected pixels from each image may be combined to create a mosaicked image for experimental tests of the proposed integrated colour correction and nonlinear demosaicking algorithm.

The advantage of using 3D printing is that it is allows for cheap and fast prototyping. The ease of designing and obtaining the printed parts ensures that the focus of the research can remain on the functionality of the image sensor components, and not on building the camera body. With a fully portable design, the colour algorithms developed in this thesis can be evaluated using real data in a relevant environment.

References

[1] M. Bae, B.-S. Choi, S.-H. Jo, H.-H. Lee, P. Choi, and J.-K. Shin, "A Linear-Logarithmic CMOS Image Sensor With Adjustable Dynamic Range," *IEEE Sensors Journal*, vol. 16, no. 13, pp. 5222–5226, 2016. DOI: 10.1109/JSEN.2016.2562638. 7, 15, 16, 34, 49

[2] B. E. Bayer, *Color imaging array*, U.S. Patent, Feb. 3, 1986. 34

[3] A. M. Brunetti and B. Choubey, "A low dark current wide dynamic range CMOS pixel," in *IEEE International Symposium on Circuits and Systems*, 2016, pp. 2523–2526. DOI: 10.1109/ISCAS.2016.7539106. 15, 16, 49

[4] P. Cambou and J.-L. Jaffard, "Status of the CMOS Image Sensors Industry," Yole Développment, Tech. Rep., 2015, pp. 1–23. [Online]. Available: http://www.yole.fr/iso_upload/Samples/Yole_CMOS_Image_Sensors_January_2015_Sample.pdf. 2, 15

[5] B. S. Carlson, "Comparison of modern ccd and cmos image sensor technologies and systems for low resolution imaging," in *SENSORS, 2002 IEEE*, vol. 1, Jun. 2002, pp. 171–176. DOI: 10.1109/ICSENS.2002.1037011. 2

[6] R. E. Carlson and F. N. Fritsch, "Monotone Piecewise Bicubic Interpolation," *SIAM Journal on Numerical Analysis*, vol. 22, no. 2, pp. 386–400, 1985. DOI: 10.1137/0722023. 8, 20

[7] D. R. Cok, *Signal processing method and apparatus for producing interpolated chrominance values in a sampled color image signal*, U.S. Patent, Jul. 20, 1976. 11

[8] F. de Souza Campos, M. M. da Silva, M. E. Bordon, and J. W. Swart, "A logarithmic cmos image sensor with wide output voltage swing range," in *2017 International Caribbean Conference on Devices, Circuits and Systems (ICCDCS)*, Jun. 2017, pp. 69–72. DOI: 10.1109/ICCDCS.2017.7959722. 7, 48

[9] F. Y. Edgeworth, "On a new method of reducing observations relating to several quantities," *The London, Edinburgh, and Dublin Philosophical Magazine and Journal of Science*, vol. 25, no. 154, pp. 184–191, 1888. 36

[10] A. El Gamal, "Trends in CMOS image sensor technology and design," in *IEEE International Electron Devices Meeting*, https://slideplayer.com/slide/5723714/, 2002, pp. 805–808. DOI: 10.1109/IEDM.2002.1175960. 23

[11] A. Ganguly, P. G. Roos, T. Simak, J. M. Yu, S. Freestone, D. Hondongwa, R. E. Colbeth, and I. P. Mollov, "X-ray performance of new high dynamic range CMOS detector," vol. 10573, 2018. [Online]. Available: http://dx.doi.org/10.1117/12.2293771. 4, 48

[12] M. Gharbi, G. Chaurasia, S. Paris, and F. Durand, "Deep joint demosaicking and denoising," *ACM Trans. Graph.*, vol. 35, no. 6, 191:1–191:12, Nov. 2016, ISSN: 0730-0301. DOI: 10.1145/2980179.2982399. 34

[13] J. Grimes and J. Hootman, "Guest editors' introduction," *IEEE Micro*, vol. 18, no. 03, pp. 8–9, 1988, ISSN: 0272-1732. DOI: 10.1109/MM.1988.10021. 2

[14] D. W. Hertel and E. Chang, "Image quality standards in automotive vision applications," 2007, pp. 404–409. 5, 6

[15] B. Hoefflinger, *High-Dynamic-Range (HDR) Vision*, ser. Advanced Microelectronics. Springer, 2007, vol. 26. [Online]. Available: https://link.springer.com/book/10.1007/978-3-540-44433-6. 4, 16, 50, 51

[16] S. Hussain and D. Joseph, "Spline-Based Colour Correction For Monotonic Nonlinear CMOS Image Sensors," Society for Imaging Science and Technology, 2019, pp. 362 1–6. 34

[17] ISO, "Graphic technology – Standard object colour spectra database for colour reproduction evaluation (SOCS)," International Organization for Standardization, Tech. Rep., 2003. [Online]. Available: https://www.iso.org/standard/37358.html. 27, 51

[18] D. Joseph and S. Collins, "Modeling, calibration, and correction of nonlinear illumination-dependent fixed pattern noise in logarithmic CMOS image sensors," *IEEE Transactions on Instrumentation and Measurement*, vol. 51, no. 5, pp. 996–1001, 2002. DOI: 10.1109/TIM.2002.807803. 8, 16, 50

[19] ——, "Modeling, calibration, and rendition of color logarithmic CMOS image sensors," *IEEE Transactions on Instrumentation and Measurement*, vol. 52, no. 5, pp. 1581–1587, 2003. DOI: 10.1109/TIM.2003.818551. 10, 16, 49–51

[20] T. Kim, "Wide dynamic range technologies: For mobile imaging sensor systems.," *IEEE Consumer Electronics Magazine*, vol. 3, no. 2, pp. 30–35, Apr. 2014. 7

[21] R. Kimmel, "Demosaicing: Image reconstruction from color ccd samples," *IEEE Trans. Image Process. (USA)*, vol. 8, no. 9, pp. 1221–8, 1999, ISSN: 1057-7149. [Online]. Available: http://dx.doi.org/10.1109/83.784434. 12, 34, 40, 52

[22] T. Latha and M. Sasikumar, "A novel non-linear transform based image restoration for removing three kinds of noises in images," *Journal of The Institution of Engineers (India): Series B*, vol. 96, no. 1, pp. 17–26, Mar. 2015, ISSN: 2250-2114. DOI: 10.1007/s40031-014-0123-y. 10

[23] J. Li, A. Mahmoodi, and D. Joseph, "Using Polynomials to Simplify Fixed Pattern Noise and Photometric Correction of Logarithmic CMOS Image Sensors," *Sensors*, vol. 15, no. 10, pp. 26 331–26 352, 2015. DOI: 10.3390/s151026331. 8, 16, 17, 19, 23, 31, 50

[24] Z. Li, X. Wang, B. Li, and Y. Chang, "160 db dynamic range pixel with charge compensation for cmos image sensor," *Electronics Letters*, vol. 52, no. 10, 819–821(2), May 2016, ISSN: 0013-5194. 7, 48

[25] Y.-C. K. Liang-Wei Lai Cheng-Hsiao Lai, "A novel logarithmic response cmos image sensor with high output voltage swing and in-pixel fixed-pattern noise reduction," *IEEE Sensors Journal*, vol. 4, no. 1, pp. 122–126, Feb. 2004. DOI: 10.1109/JSEN.2003.820339. 7

[26] A. Mahmoodi, J. Li, and D. Joseph, "Digital Pixel Sensor Array with Logarithmic Delta-Sigma Architecture," *Sensors*, vol. 13, no. 8, pp. 10 765–10 782, 2013. DOI: 10.3390/s130810765. 14, 16, 24, 27, 34, 51

[27] H. S. Malvar, L.-w. He, and R. Cutler, "High-quality linear interpolation for demosaicing of Bayer-patterned color images," in *IEEE International Conference on Acoustics, Speech, and Signal Processing*, vol. 3, 2004, pp. iii-485–488. DOI: 10.1109/ICASSP.2004.1326587. 12, 13, 18, 21, 34, 40, 50

[28] K. Martišek and H. Druckmüllerová, "A numerical method for the visualization of the Fe XIV emission in the solar corona using broadband filters," *The Astrophysical Journal Supplement Series*, vol. 197, no. 23, pp. 1–7, 2011. DOI: 10.1088/0067-0049/197/2/23. 23

[29] C. S. McCamy, H. Marcus, and J. G. Davidson, "A Color-Rendition Chart," *Journal of Applied Photographic Engineering*, vol. 2, no. 3, pp. 95–99, 1976. [Online]. Available: https://publiclab.org/system/images/photos/000/004/361/original/mccamy1976.pdf. 25, 51

[30] G. Melotti, C. Premebida, N. M. S. Goncalves, U. Nunes, and D. R. Faria, "Multimodal cnn pedestrian classification: A study on combining lidar and camera data," 2018, pp. 3138–3143. [Online]. Available: http://dx.doi.org/10.1109/ITSC.2018.8569666. 6

[31] M. Nascimento, J. Li, and D. Joseph, "Digital circuit methods to correct and filter noise of nonlinear cmos image sensors," *Journal of Imaging Science and Technology*, vol. 62, no. 6, 2018. [Online]. Available: http://dx.doi.org/10.2352/J.ImagingSci.Technol.2018.62.6.060404. 8, 9, 35, 49, 52, 55

[32] A.-C. Peter, M. Schnaubelt, and M. Gente, "Multispectral x-ray imaging to distinguish among dental materials," *Imaging Science in Dentistry*, vol. 47, no. 4, pp. 247–254, 2017. DOI: 10.5624/isd.2017.47.4.247. 5, 48

[33] S. Plainis, I. J. Murray, and I. G. Pallikaris, "Road traffic casualties: Understanding the night-time death toll," *Injury Prevention*, vol. 12, no. 2, pp. 125–138, 2006, ISSN: 1353-8047. DOI: 10.1136/ip.2005.011056. 5

[34] C. Poynton, *Digital Video and HD: Algorithms and Interfaces*, ser. The Morgan Kaufmann Series in Computer Graphics. Elsevier, 2012. DOI: 10.1016/C2010-0-68987-5. 25

[35] M. Selek, "A new autofocusing method based on brightness and contrast for color cameras," *Adv. Electr. Comput. Eng*, vol. 16, no. 4, pp. 39–44, 2016. 12

[36] G. Sharma and R. Bala, *Digital Color Imaging Handbook*. CRC Press, 2017. DOI: 10.1201/9781420041484. 25, 51

[37] O. Skorka and D. Joseph, "Toward a digital camera to rival the human eye," *Journal of Electronic Imaging*, vol. 20, no. 3, pp. 1–18, 2011. DOI: 10.1117/1.3611015. [Online]. Available: https://doi.org/10.1117/1.3611015. 2, 3

[38] G. P. Stein, O. Mano, and A. Shashua, "Vision-based acc with a single camera: Bounds on range and range rate accuracy," 2003, pp. 120–125. [Online]. Available: http://dx.doi.org/10.1109/IVS.2003.1212895. 6

[39] M. Stokes, M. Anderson, S. Chandrasekar, and R. Motta, "A Standard Default Color Space for the Internet – sRGB," Microsoft and Hewlett-Packard, Tech. Rep., 1996. [Online]. Available: https://www.w3.org/Graphics/Color/sRGB. 25

[40] T. Suzuki, "Challenges of image-sensor development," in *2010 IEEE International Solid-State Circuits Conference - (ISSCC)*, Feb. 2010, pp. 27–30. DOI: 10.1109/ISSCC.2010.5434065. 2, 48

[41] M. Tektonidis, M. Pietrzak, and D. Monnin, "Evaluation of a logarithmic hdr sensor for an image-based navigation system," vol. 10643, 2018. [Online]. Available: http://dx.doi.org/10.1117/12.2304887. 6

[42] X. Wang, W. Lin, and P. Xue, "Demosaicing with improved edge direction detection," Kobe, Japan, 2005, pp. 2048–2051. [Online]. Available: http://dx.doi.org/10.1109/ISCAS.2005.1465020. 34, 40, 52

[43] S. Yang, X. Zhuang, F. Xue, Q. Sun, and N. Ruan, "Imaging performance comparison of novel cmos low-light-level image sensor and electron multiplying ccd sensor," in *SENSORS, 2002 IEEE*, vol. 10462, 2017, pp. 171–176. DOI: 10.1117/12.2285297. 2

[44] Yap-Peng Tan and T. Acharya, "A robust sequential approach for the detection of defective pixels in an image sensor," in *1999 IEEE International Conference on Acoustics, Speech, and Signal Processing. Proceedings*, vol. 4, Mar. 1999, pp. 2239–2242. DOI: 10.1109/ICASSP.1999.758382. 9, 35, 52

[45] G. Zentai, "Comparison of cmos and a-si flat panel imagers for x-ray imaging," 2011, pp. 194–200. [Online]. Available: http://dx.doi.org/10.1109/IST.2011.5962217. 4